Nuclear Engineering and Design 404 (2023) 112159

Contents lists available at ScienceDirect

Nuclear Engineering and Design

journal homepage: www.elsevier.com/locate/nucengdes

A numerical study of the MRT-LBM for the shallow water equation in high Reynolds number flows: An application to real-world tsunami simulation

Kenta Sato [a,*], Koji Kawasaki [b,c], Shunichi Koshimura [d]

[a] Hydro Technology Institute Co., Ltd., Nakanoshima 3-3-23, Kita-ku, Osaka, Japan
[b] KK Technical Research Institute, Nagoya, Japan
[c] Department of Civil Engineering, Meijo University, Shiogamaguchi 1-501, Tempaku-ku, Nagoya, Japan
[d] International Research Institute of Disaster Science, Tohoku University, Aoba 468-1, Aramaki, Aoba-ku, Sendai, Japan

ARTICLE INFO

Keywords:
Lattice Boltzmann method
MRT model
Shallow water flows
High Reynolds number flows
Tsunami simulation

ABSTRACT

The lattice Boltzmann method (LBM) has recently attracted attention as a simple computational fluid dynamics (CFD) method that does not directly solve macroscopic equations. Due to the advantage of its local scheme, the LBM is expected to efficiently achieve highly accurate and high-resolution fluid simulations. In particular, the application of the LBM to disaster simulations has been studied since the proposal of the LBM for nonlinear shallow water equations (LABSWE). However, it is well known that the LBM is prone to computational instability in high Reynolds number flows. A tsunami inundating an urban area is considered a high Reynolds number flow because of its violent flow. The numerical stability in such flows must be enhanced for the application of the LBM to real-world tsunami simulations. For this purpose, it is practical to introduce the subgrid-scale (SGS) model into the multiple-relaxation-time (MRT) model. Notably, the MRT model is computationally more expensive than the conventional lattice Bhatnagar–Gross–Krook (BGK) model. In this study, we modified the SGS model for the MRT model. We verified the calculation accuracy by focusing on grid size differences in the classical benchmark problems in high Reynolds number flows. Finally, we simulated the 2011 tsunami off the Pacific coast caused by the Tohoku earthquake. The LBM simulations reproduced the tsunami propagation waveform and inundation depth with the computational accuracy equally as good as that of the finite difference method (FDM).

1. Introduction

The 2011 Tohoku earthquake off the Pacific coast caused considerable human and economic damage in Japan. Most of this damage was caused by the tsunami, which was much larger than expected. The tsunami struck the coast, spread beyond the estimated inundation zone announced by the local government, and overwhelmed many people and houses. This tsunami disaster has shown that external forces beyond the expected range can cause critical damage. Furthermore, the tsunami entered the Fukushima Daiichi nuclear power plant and was the leading cause of damage related to this major nuclear accident.

Although many factors contributed to the accident, the direct trigger was undoubtedly the arrival of the tsunami. Thus, underestimation of the tsunami was a factor in the accident. A further problem was the inadequate preparation of the nuclear power plant for the situation that would arise from this tsunami. The damage caused by a nuclear accident is pervasive and long-lasting. Nuclear power plants must be designed with sufficient safety margins (Saji, 2014). A hardware safety design approach is necessary to apply the lessons learned from the disaster in the future.

Various tsunami hazard assessment studies have been conducted in the field of nuclear engineering. Ghosh (2008) studied the tsunami hazard at a power plant site on the east coast of India and discussed various tsunami sources based on crustal information, past earthquakes, and tsunami records. Ebisawa et al. (2015) proposed the concept of core damage frequency as a tsunami countermeasure in nuclear power plants, considering multiple units and site failures. These are practical approaches for considering many scenarios and estimating tsunami hazards over a wide area.

Physically based tsunami hazard assessment for each hardware component conducted by using hydraulic experiments and fluid simulations is also important. Many studies using various simulation methods have been reported. Morikawa et al. (2020) proposed explicit incompressible smoothed particle hydrodynamics (EISPH) and successfully performed three-dimensional tsunami inundation simulations at the Fukushima

* Corresponding author.
E-mail addresses: satokt@hydrosoken.co.jp (K. Sato), kawasaki@nagoya-u.jp (K. Kawasaki), koshimura@irides.tohoku.ac.jp (S. Koshimura).

https://doi.org/10.1016/j.nucengdes.2023.112159
Received 13 December 2021; Received in revised form 10 December 2022; Accepted 7 January 2023
Available online 16 January 2023
0029-5493/© 2023 The Author(s). Published by Elsevier B.V. This is an open access article under the CC BY-NC-ND license (http://creativecommons.org/licenses/by-nc-nd/4.0/).

Daiichi nuclear power plant. Vallée et al. (2010) conducted an experiment on the backflow control of hydraulic jumps that are essential for the operation of nuclear reactors. They also proposed a benchmark problem to validate computational fluid dynamics (CFD) codes. Kimura et al. (2017) investigated the inundation damage from the exterior wall ventilation of a nuclear power plant using a wall flap gate. They also performed hydraulic experiments and found that the wall flap gate was an excellent stopping structure to protect nuclear power plants from tsunami inundation. Moriyama and Furuya (2020) used the water vapour explosion simulation code JASMINE to investigate water vapour explosion in a shallow water pool. Podila et al. (2020) focused on the modelling, solidification, and redistribution of core melts to simulate corium relocation in a hypothetical accident. Due to the harsh environment of nuclear power production, these phenomena are not easy to understand via experiments. Numerical simulation is an advantageous method for physically-based hazard assessments, such as severe tsunami accident prevention in nuclear power plants.

Since these examples are three-dimensional and strongly nonlinear problems, it is necessary to conduct nonhydrostatic fluid simulations. Furthermore, a two-dimensional hydrostatic model is important because tsunami propagation and inundation are widespread phenomena. Cho et al. (2004) simulated the tsunami caused by the 1983 Nihonkai-Chubu earthquake using a two-dimensional model based on nonlinear long-wave theory. They calculated the maximum run-up height of the tsunami at the Hanul nuclear power plant and compared it with the observed data to investigate the safety of the power plant. Bladé et al. (2019) used nonlinear shallow water equations discretized by the finite volume method (FVM) to simulate the flooding process in the service gallery that occurred when the pipes of the essential services water system (ESWS) failed.

Most conventional fluid simulation methods are based on the discretization of the macroscopic governing equations by the FVM, finite difference method (FDM) or mesh-free particle method (Lucy, 1977; Gingold and Monaghan, 1977; Koshizuka and Oka, 1996). The lattice Boltzmann method (LBM) has attracted attention as an alternative fluid simulation method. The LBM has the following features:

- The algorithm is simple and easy to code.
- Since the LBM is a local computation scheme, it is suitable for parallel computation using computational coprocessors such as GPUs (Janßen and Krafczyk, 2011; Rinaldi et al., 2012; Obrecht et al., 2012, 2013; Koda and Lien, 2015; Calore et al., 2016).

In the fields of nuclear energy and ocean engineering, the LBM has attracted substantial attention (Ohashi et al., 1995) since it was first proposed (McNamara and Zanetti, 1988; Chen et al., 1992; Chen and Doolen, 1998). Both application studies and theoretical studies (Nourgaliev et al., 2002) have been conducted. Although the LBM was originally used to solve the Navier–Stokes (NS) equation, it can be easily extended. A model to calculate the thermal convection (Yoshida and Nagaoka, 2010; Wang et al., 2013; Li et al., 2014; Gao et al., 2014; Li et al., 2016; Wang et al., 2017), a single-phase free-surface model for violent flow fields (Janssen and Krafczyk, 2010; Janßen and Krafczyk, 2011; Janßen et al., 2013; Sato and Koshimura, 2020; Sato et al., 2022) and a two-phase flow model (He et al., 1999; Lee and Lin, 2005; Inamuro et al., 2016, 2018) have been proposed and applied. Chen et al. (2007) simulated natural convection using the LBM of heat transfer. They investigated the oxygen transport mechanism for suppressing the corrosion of a lead–bismuth eutectic. Hussein et al. (2014) simulated the natural convection of a Cu–water nanofluid in an open enclosure and numerically investigated its magnetohydrodynamic properties. Yang et al. (2001) numerically studied pool boiling behaviour using the two-phase LBM code FlowLab. Ryu and Ko (2012), Ryu et al. (2014), and Ryu et al. (2016) simulated pool boiling using the two-phase LBM based on the free energy model (Zheng et al., 2006) and simulated rising bubbles in a low-viscosity liquid considering the instability of the path of two rising bubbles. Tiftikçi and Kocar (2016) numerically investigated turbulence using the LBM model and studied the relationship between the grid size and calculation accuracy in detail. As described above, the LBM excels in solving many problems in the nuclear engineering field.

Although the nonhydrostatic three-dimensional free-surface flow model is required to accurately simulate the velocity and pressure of tsunamis, hydrostatic pressure provides a good approximation for shallow water tsunami propagation and inundation simulations. Based on this, the LBM for nonlinear shallow water equations has attracted considerable attention as a new tsunami propagation and inundation simulation model. It was formulated as the LABSWE by Zhou (2004). The LABSWE has been studied and developed by many researchers (Thömmes et al., 2007; Klar et al., 2008; Liu et al., 2010a; Zhou and Borthwick, 2011; Liu et al., 2015). These studies include the introduction of the multiple-relaxation-time (MRT) model (Liu et al., 2012; Peng et al., 2014) and the turbulence model (Zhou, 2002; Liu et al., 2012), treatment of bed-slope gradients (Zhou, 2011; Zhou and Liu, 2013; Li et al., 2015), and development of moving boundary conditions (Frandsen, 2008; Liu and Zhou, 2014; Liu et al., 2016, 2017). LABSWE was also applied to tsunami simulations. Shafiai et al. (2021) proposed a tsunami simulation model by introducing a non-Newtonian fluid model into the LABSWE and successfully applied it to tsunami propagation and inundation simulations.

The MRT model (Lallemand and Luo, 2000; D'Humières et al., 2002) is stable in high Reynolds number flows (Janßen and Krafczyk, 2011). In the lattice Bhatnagar–Gross–Krook (BGK) model (Bhatnagar et al., 1954; Qian et al., 1992), numerical oscillations occur in high Reynolds number flows with small kinematic viscosity because the kinematic viscosity and bulk viscosity are equal. However, the kinematic and bulk viscosities can be set independently in the MRT model. Numerical oscillations due to acoustic errors can be suppressed. Therefore, the MRT model is suitable for simulating violent flow fields. Liu et al. (2012) successfully applied large-eddy simulation (LES) based on the subgrid-scale (SGS) model to the MRT model. They found that the MRT model is superior to the BGK model in terms of computational accuracy and stability. However, the MRT model had an increased computational cost compared with that of the BGK model because of its slightly complex computational algorithm.

In this study, the turbulence model for the MRT model with the LABSWE (MRT-LABSWE) (Liu et al., 2012) is first modified. The modified model is applied to the dam break flow that flows around a square cylinder (Lyn et al., 1995) and cavity flow (Ghia et al., 1982; Erturk et al., 2005; Bruneau and Saad, 2006) to verify the applicability of the model to high Reynolds number flow problems. The relationship between the numerical oscillations and the grid size is verified by comparison with the BGK model. Finally, the 2011 tsunami off the Pacific coast caused by the Tohoku earthquake is simulated using the proposed model. Various simulations of this tsunami event have been reported using existing models, such as the shallow water (Oishi et al., 2015) or Boussinesq wave model (Grilli et al., 2013; Kirby et al., 2013; Ha and Cho, 2015; Baba et al., 2015). In addition, Janßen et al. (2015) simulated this tsunami by using the LABSWE. However, verification of the accuracy of such an inundation depth or propagation waveform in an actual tsunami event remains challenging. We demonstrate that the LABSWE can simulate real-world tsunami propagation and inundation with a computational accuracy identical to that of the existing shallow water model discretized by the FDM.

The structure of this paper is as follows. Section 2 provides the basic theory for the nonlinear shallow water equations of the LBM. We also present the modified SGS model for the MRT model here. Section 3 describes the calculation schemes required to perform real-world tsunami simulations by the LBM. Section 4 verifies the MRT model with the SGS model in some benchmark problems. Section 5 applies the LBM to the simulations of the 2011 tsunami off the Pacific coast caused by the Tohoku earthquake and compares the obtained results with the FDM results. Section 6 concludes this paper.

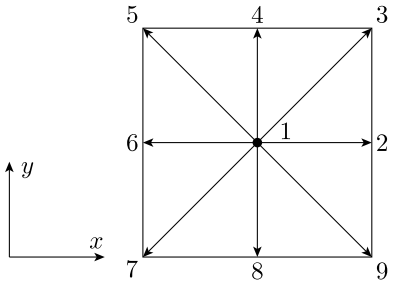

Fig. 1. The two-dimensional nine-speed (D2Q9) lattice model.

2. Lattice Boltzmann method for shallow water equations

2.1. Basic theory of the shallow water model

When the horizontal motion of water particles is much larger than the vertical scale, the vertical acceleration is negligible compared to the gravitational acceleration and the pressure distribution is assumed to be hydrostatic. Based on these approximations, depth-averaged NS equations can be considered as a shallow water model. The equations for the conservation of mass and momentum in tensor form are given as:

$$\frac{\partial h}{\partial t} + \frac{\partial \left(hu_j\right)}{\partial x_j} = 0, \tag{1}$$

$$\frac{\partial \left(hu_i\right)}{\partial t} + \frac{\partial \left(hu_iu_j\right)}{\partial x_j} = F_i - g\frac{\partial}{\partial x_i}\left(\frac{h^2}{2}\right) + \nu\frac{\partial^2 \left(hu_i\right)}{\partial x_j \partial x_j}, \tag{2}$$

where subscripts i and j are indices, to which the Einstein summation rule is applied. Here, we consider the XY plane. x_j is a Cartesian coordinate; $g = 9.81\ \mathrm{m/s^2}$ is gravitational acceleration; h is the total water depth; u_j is the depth-averaged velocity; ν is the kinetic viscosity; and F_i is an external force term. When the wind shear stress and Coriolis force are negligible, F_i is defined as:

$$F_i = -gh\frac{\partial z_b}{\partial x_i} - \frac{\tau_{bi}}{\rho}, \tag{3}$$

where ρ is the density; z_b is the bottom bed elevation; and τ_{bi} is the bed shear stress in the i direction that is determined from the depth-averaged velocities as follows:

$$\tau_{bi} = \rho C_b u_i \sqrt{u_j u_j}, \tag{4}$$

where C_b is the bed friction coefficient that is estimated as:

$$C_b = \frac{g}{C_z^2}. \tag{5}$$

Here, C_z is the Chezy coefficient given by the Manning equation:

$$C_z = \frac{h^{1/6}}{n}, \tag{6}$$

where n is Manning's coefficient.

2.2. BGK model for shallow water equations (BGK-LABSWE)

The LABSWE is derived from lattice gas automata for molecular dynamics based on mesoscopic kinematic equations, where the particle distribution functions f_α are used to simulate fluid dynamics. The solution of the LABSWE is guaranteed to have second-order accuracy in space (Zhou, 2004) by the Chapman–Enskog expansion in finite Knudsen numbers. In this study, we used the two-dimensional nine-speed (D2Q9) lattice model in Fig. 1 to discretize the continuous Boltzmann equation. Each particle distribution function f_α streams one lattice unit at its corresponding velocity along one of the eight links indicated by indices 2–9. The index of 1 indicates a particle at rest. The velocity vector e_α for the particles in the α link is given by:

$$e_\alpha = \begin{cases} (0,0), & (\alpha = 1), \\ e\left[\cos\frac{(\alpha-1)\pi}{4}, \sin\frac{(\alpha-1)\pi}{4}\right], & (\alpha = 2,4,6,8), \\ \sqrt{2}e\left[\cos\frac{(\alpha-1)\pi}{4}, \sin\frac{(\alpha-1)\pi}{4}\right], & (\alpha = 3,5,7,9), \end{cases} \tag{7}$$

where $e = \Delta x/\Delta t$. Δx is the grid size; Δt is the time step interval.

The lattice BGK equation is widely used as a simple governing equation of the LABSWE (BGK-LABSWE). The BGK-LABSWE including the external force term F_j is given as:

$$f_\alpha\left(x_i + e_\alpha\Delta t, t + \Delta t\right) = f_\alpha\left(x_i, t\right) - \frac{1}{\tau}\left[f_\alpha\left(x_i, t\right) - f_\alpha^{eq}\left(h, u_i\right)\right] + W_\alpha\frac{3}{e^2}e_{\alpha j}F_j\left(x_i, t\right)\Delta t, \tag{8}$$

where f_α^{eq} is the local equilibrium distribution function and τ is the relaxation time. In this equation, the weighting factor method (Thömmes et al., 2007) is used to calculate the effects of external forces, where the weighting parameter W_α in the D2Q9 model is given as Liu et al. (2012):

$$W_\alpha = \begin{cases} \frac{1}{9}, & (\alpha = 2,4,6,8), \\ \frac{1}{36}, & (\alpha = 3,5,7,9). \end{cases} \tag{9}$$

The BGK-LABSWE uses a single relaxation rate for the collision of all distribution functions f_α. The relaxation time τ is defined by the kinematic viscosity ν as follows:

$$\tau = 3\nu\frac{\Delta t}{\Delta x^2} + \frac{1}{2}. \tag{10}$$

It is important to determine suitable equilibrium distribution functions f_α^{eq} for the LBM because this function determines the flow equation that can be solved by the lattice Boltzmann equation. To solve the shallow water equations in the D2Q9 model, Zhou (2004) proposed the following equilibrium functions:

$$f_\alpha^{eq} = \begin{cases} h - \frac{5gh^2}{6e^2} - \frac{2h}{3e^2}u_iu_i, & (\alpha = 1), \\ \frac{gh^2}{6e^2} + \frac{h}{3e^2}e_{\alpha i}u_i + \frac{h}{2e^4}e_{\alpha i}e_{\alpha j}u_iu_j - \frac{h}{6e^2}u_iu_i, & (\alpha = 2,4,6,8), \\ \frac{gh^2}{24e^2} + \frac{h}{12e^2}e_{\alpha i}u_i + \frac{h}{8e^4}e_{\alpha i}e_{\alpha j}u_iu_j - \frac{h}{24e^2}u_iu_i, & (\alpha = 3,5,7,9), \end{cases} \tag{11}$$

where the total water depth h and depth-averaged velocity u_i are defined by the 0th- and 1st-order moments of the distribution function f_α:

$$h = \sum_{\alpha=1}^{9} f_\alpha, \tag{12}$$

$$u_i = \frac{1}{h}\sum_{\alpha=1}^{9} e_{\alpha i}f_\alpha. \tag{13}$$

2.3. MRT model for shallow water equations (MRT-LABSWE)

The MRT-LABSWE utilizes an individual relaxation rate for each moment space $\boldsymbol{m}$ in the particle collision. The governing equation of the MRT-LABSWE is given by Lallemand and Luo (2000), D'Humières et al. (2002), Liu et al. (2012), Peng et al. (2014):

$$f_\alpha\left(x_i + e_\alpha\Delta t, t + \Delta t\right) - f_\alpha\left(x_i, t\right) = -\mathbf{M}^{-1}\hat{\mathbf{S}}\left[\mathbf{M}\cdot f_\alpha\left(x_i, t\right) - m_\alpha^{eq}\left(x_i, t\right)\right] + W_\alpha\frac{3}{e^2}e_{\alpha j}F_j\left(x_i, t\right)\Delta t. \tag{14}$$

where $\mathbf{M}$ is the 9×9 matrix that transforms the velocity distribution functions f_α into the moment distribution functions m_α. Matrix $\mathbf{M}$ must satisfy the following requirements:

$$m_\alpha = \mathbf{M}\cdot f_\alpha, \quad f_\alpha = \mathbf{M}^{-1}\cdot m_\alpha, \tag{15}$$

and matrix **M** for the D2Q9 lattice model is given as follows (Lallemand and Luo, 2000):

$$\mathbf{M} = \begin{bmatrix} 1 & 1 & 1 & 1 & 1 & 1 & 1 & 1 & 1 \\ -4 & -1 & 2 & -1 & 2 & -1 & 2 & -1 & 2 \\ 4 & -2 & 1 & -2 & 1 & -2 & 1 & -2 & 1 \\ 0 & 1 & 1 & 0 & -1 & -1 & -1 & 0 & 1 \\ 0 & -2 & 1 & 0 & -1 & 2 & -1 & 0 & 1 \\ 0 & 0 & 1 & 1 & 1 & 0 & -1 & -1 & -1 \\ 0 & 0 & 1 & -2 & 1 & 0 & -1 & 2 & -1 \\ 0 & 1 & 0 & -1 & 0 & 1 & 0 & -1 & 0 \\ 0 & 0 & 1 & 0 & -1 & 0 & 1 & 0 & -1 \end{bmatrix}. \tag{16}$$

Therefore, the collision of the MRT-LABSWE consists of the following three calculation steps.

1. Transformation of the velocity distribution functions f_α into moment distribution functions m_α.
2. Collision for each moment space $\boldsymbol{m}$ using independent relaxation rates.
3. Inverse transformation of the moment distribution functions m_α into the velocity distribution functions f_α.

In the MRT model, the moment distribution functions m_α are written as:

$$m_\alpha = \left(\rho, e, \epsilon, j_x, q_x, j_y, q_y, p_{xx}, p_{xy}\right), \tag{17}$$

where ρ is the density and j_x and j_y are the momenta. These are conserved variables. The remaining moments are the nonconserved variables, and their equilibria are functions of the conserved moments. The moment equilibrium functions m_α^{eq} can be expressed as Liu et al. (2012), Peng et al. (2014):

$$m_\alpha^{eq} = \begin{cases} h, & (\alpha = 1), \\ -4h + \dfrac{3gh^2}{e^2} + \dfrac{3h\left(u^2+v^2\right)}{e^2}, & (\alpha = 2), \\ 4h - \dfrac{9gh^2}{2e^2} - \dfrac{3h\left(u^2+v^2\right)}{e^2}, & (\alpha = 3), \\ \dfrac{hu}{e}, & (\alpha = 4), \\ -\dfrac{hu}{e}, & (\alpha = 5), \\ \dfrac{hv}{e}, & (\alpha = 6), \\ -\dfrac{hv}{e}, & (\alpha = 7), \\ \dfrac{h\left(u^2-v^2\right)}{e^2}, & (\alpha = 8), \\ \dfrac{huv}{e^2}, & (\alpha = 9). \end{cases} \tag{18}$$

$\hat{\mathbf{S}}$ is the diagonal collision matrix, which consists of the individual relaxation rates as given by:

$$\hat{\mathbf{S}} = \mathrm{diag}\left(s_1, s_2, s_3, s_4, s_5, s_6, s_7, s_8, s_9\right), \tag{19}$$

where s_8 and s_9 are related to the relaxation time τ as follows:

$$s_8 = s_9 = \frac{1}{\tau}, \tag{20}$$

and the bulk viscosity ζ is given as Tubbs and Tsai (2019):

$$\zeta = \frac{1}{6}\left(\frac{1}{s_1} - \frac{1}{2}\right)\frac{\Delta x^2}{\Delta t}. \tag{21}$$

With the exception of s_8 and s_9, the relaxation parameters can be flexibly determined. In this study, we set these values equal to 1 (Peng et al., 2014).

The MRT-LABSWE has the advantage that the bulk viscosity ζ can be increased by setting a different parameter from the kinematic viscosity ν. The LBM shows good numerical stability when the bulk viscosity ζ is larger than the kinematic viscosity ν (Ramshaw and Mousseau, 1990; Dellar, 2001; Sato et al., 2022). In the BGK-LABSWE, the bulk viscosity ζ is given by 2ν (Tubbs and Tsai, 2019), and ζ becomes small for high Reynolds number flows. As a result, numerical stability is reduced. On the other hand, the MRT-LABSWE is suitable for high Reynolds number flows because ζ can be set larger than ν by Eq. (21).

2.4. Turbulence modelling

In high Reynolds number flows, the relaxation time τ is close to 0.5 according to Eq. (10). In the LBM, it is known that numerical instability tends to occur when τ approaches 0.5. Therefore, it is common to introduce eddy viscosity by a turbulence model for high Reynolds number flows to increase numerical stability. This is not only for LABSWE but also for free-surface flow models. There have been reports of stable simulations for violent free-surface flows such as dam break by introducing a turbulence model (Janssen and Krafczyk, 2010; Janßen et al., 2013; Sato and Koshimura, 2020; Sato et al., 2022).

In this study, a turbulence model is further applied to enhance the numerical stability of LABSWE. Thus, the relaxation time τ is increased by adding the eddy viscosity ν_e to the kinematic viscosity ν. Zhou (2002) proposed a turbulent model based on the standard Smagorinsky subgrid scale (SGS) model in combination with BGK-LABSWE. The combination of BGK-LABSWE and the turbulence model has been successfully applied to simulate turbulent flows in a meandering channel flow (Liu et al., 2009) and a partial dam break (Liu et al., 2010b).

In the SGS model, the total viscosity ν_t can be expressed as the sum of the eddy viscosity ν_e and kinematic viscosity ν as follows:

$$\nu_t = \nu + \nu_e. \tag{22}$$

It is noted that by considering ν as ν_t in Eq. (2), the eddy viscosity is taken into account. The eddy viscosity ν_e is defined as:

$$\nu_e = \left(c_s l_s\right)^2 \sqrt{S_{ij} S_{ij}}, \tag{23}$$

where c_s is the Smagorinsky constant. We set $c_s = 0.3$ in this study. l_s is the characteristic length scale, which is equal to Δx. S_{ij} is the magnitude of the large-scale strain rate tensor defined as:

$$S_{ij} = \frac{1}{2h}\left[\frac{\partial\left(hu_i\right)}{\partial x_j} + \frac{\partial\left(hu_j\right)}{\partial x_i}\right], \tag{24}$$

The depth-averaged SGS stress τ_{ij} is calculated as:

$$\tau_{ij} = -2h\nu_e S_{ij}. \tag{25}$$

The total relaxation time τ_t with the eddy viscosity in LABSWE is simply calculated by adding the eddy relaxation time τ_e to the relaxation time τ as follows:

$$\tau_t = \tau + \tau_e, \tag{26}$$

where the eddy relaxation time τ_e can be calculated as:

$$\tau_e = \frac{-\tau + \sqrt{\tau^2 + 18c_s^2/\left(e^2 h\right)\sqrt{\Pi_{ij}\Pi_{ij}}}}{2}, \tag{27}$$

where Π_{ij} is a non-equilibrium tensor defined as Liu et al. (2012):

$$\Pi_{ij} = \sum_{\alpha=1}^{9} e_{\alpha i} e_{\alpha j}\left(f_\alpha - f_\alpha^{eq}\right). \tag{28}$$

Hence, the total relaxation time τ_t is given as:

$$\tau_t = \tau + \tau_e = \frac{\tau + \sqrt{\tau^2 + 18c_s^2/\left(e^2 h\right)\sqrt{\Pi_{ij}\Pi_{ij}}}}{2}. \tag{29}$$

Accordingly, the eddy viscosity ν_e is always positive and acts to stabilize the simulation.

In the MRT-LABSWE, the relaxation times related to the kinematic viscosity can be calculated as follows:

$$s_8 = s_9 = \frac{1}{\tau + \tau_e} = \frac{1}{\tau_t}. \tag{30}$$

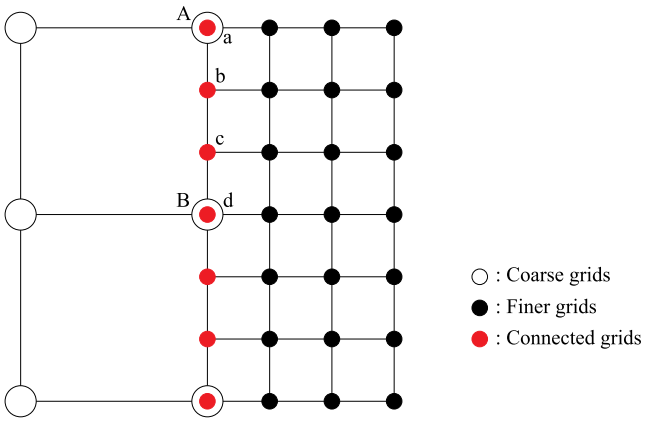

Fig. 2. Schematic diagram of the multidomain connection method. Points A and B are large-grid-size grid points, and a, b, c, and d are small-grid-size grid points.

In this study, a modified Eq. (28) for the MRT-LABSWE is considered. As mentioned above, the MRT-LBM does not have to calculate equilibrium distribution functions f_α^{eq}; rather, it computes the moment equilibrium functions m_α^{eq}. Therefore, we must calculate f_α^{eq} only for Eq. (28) in the MRT-LABSWE (Liu et al., 2012).

To obtain the equivalent results of Eq. (28) without calculating f_α^{eq}, we adopt the idea of the non-equilibrium parts of moment functions m_α^{neq} of the MRT model (Krafczyk et al., 2003) into MRT-LABSWE as follows:

$$m_\alpha^{neq} = m_\alpha - m_\alpha^{eq}. \tag{31}$$

The 2nd-order tensor operator $e_{\alpha i}e_{\alpha j}$ can be expressed as a linear superposition of the orthogonal basis vectors ϕ_β dual to the eigenvectors of the matrix **M**. We linearly transform Eq. (31) to obtain the same variables as in Eq. (28):

$$e_{ix}e_{ix} = \frac{e^2}{6}\left(4\phi_1 + \phi_2 + 3\phi_8\right), \tag{32}$$

$$e_{iy}e_{iy} = \frac{e^2}{6}\left(4\phi_1 + \phi_2 - 3\phi_8\right), \tag{33}$$

$$e_{ix}e_{iy} = e^2\phi_9. \tag{34}$$

Finally, the components of the 2nd-order tensor can be explicitly written by the non-equilibrium parts m_α^{neq} as follows:

$$\Pi_{xx} = \frac{e^2}{6}\left(4m_1^{neq} + m_2^{neq} + 3m_8^{neq}\right), \tag{35}$$

$$\Pi_{yy} = \frac{e^2}{6}\left(4m_1^{neq} + m_2^{neq} - 3m_8^{neq}\right), \tag{36}$$

$$\Pi_{xy} = e^2 m_9^{neq}. \tag{37}$$

The eddy relaxation rates can be calculated using Eq. (27) in the same manner as in BGK-LABSWE after the calculation of Eqs. (35), (36) and (37).

3. LBM for real-world tsunami simulation

In addition to the basic LBM equations described above, several calculation schemes are required to perform real-world tsunami simulations. In this section, the multidomain connection method, composite equivalent roughness model and moving boundary condition are outlined.

3.1. Multidomain connection method

In real-world tsunami simulations, the nesting connection method is generally used to improve the spatial resolution from offshore to inundation areas. In this study, we adopted the grid size ratio of the 1 : 3 connection in the LBM.

Two-way coupling is performed from a region with a large-grid-size domain to a small-grid-size domain and vice versa. Fig. 2 shows a schematic diagram of the multidomain connection method. We implement two-way coupling by linearly interpolating the macroscopic variables at the overlapping grid points between the large- and small-grid domains, indicated by the red grids in the figure. The connection from a large-grid-size domain to a small-grid-size domain is implemented via linear interpolation of the water depth h and velocity u_i. The distribution function f_α is initialized by the equilibrium distribution function f_α^{eq} from the interpolated variables. The connection from a small-grid-size domain to a large-grid-size domain is carried out by taking the average variables of nine small domain grids in the large-size grid. The distribution function f_α is also initialized by the equilibrium distribution function f_α^{eq}.

3.2. Composite equivalent roughness model

The composite equivalent roughness model (ERM) (Imai et al., 2013) is employed for the resistance of building structures in inundation simulation. This model uses digital elevation model data and the composite equivalent roughness coefficient given by Eq. (38) according to land use and building conditions:

$$n_{\mathrm{erm}} = \sqrt{\frac{100-\theta}{100}n_0^2 + \frac{\theta}{100}\frac{C_D}{2gk}h^{4/3}}, \tag{38}$$

where n_0 is the roughness coefficient according to MLIT (MLIT, 2009) ($n_0 = 0.025$ in urban areas, $n_0 = 0.03$ otherwise); θ is the percentage of the building (e.g., house) area in the calculation grid; C_D is the drag coefficient ($C_D = 0.5$ in this paper); g is the gravitational acceleration; k is the horizontal scale of houses; and h is the total water depth. Because the LABSWE uses Manning's roughness coefficients to calculate the roughness, the ERM is easy to implement.

3.3. Moving shoreline algorithm

Solutions of the nonlinear shallow water equations are only valid for a water depth h greater than zero. However, there will be areas of tsunami wave runup-rundown where parts of the computational domain are successively wetting and drying. A numerical treatment of such drying or wetting boundaries is needed. In this study, we adopt the simple linear extrapolation method (Imamura, 1996) for the LBM. This approach leads to accurate results for tsunami modelling.

Fig. 3 shows the moving boundary condition of the wavefront. This boundary condition is a simple algorithm of linear extrapolation from the difference between bed height z_b and water depths h given by:

$$h\left(\boldsymbol{x} + \boldsymbol{e}_\alpha \Delta t\right) = \begin{cases} z_b(\boldsymbol{x}) + h(\boldsymbol{x}) - z_b\left(\boldsymbol{x} + \boldsymbol{e}_\alpha \Delta t\right), & \left(z_b(\boldsymbol{x}) + h(\boldsymbol{x}) > z_b\left(\boldsymbol{x} + \boldsymbol{e}_\alpha \Delta t\right) + \delta\right), \\ 0, & \left(z_b(\boldsymbol{x}) + h(\boldsymbol{x}) \le z_b\left(\boldsymbol{x} + \boldsymbol{e}_\alpha \Delta t\right) + \delta\right), \end{cases} \tag{39}$$

where δ is an appropriate threshold value used to avoid division by zero. We set $\delta = 1.0 \times 10^{-5}$ in this study. When the water overflows a grid, the neighbouring drying grid is activated and converted to a wetting grid. The velocity is not extrapolated and is initialized as zero to avoid the numerical instability caused by the extrapolation of large velocity to small water depth. The distribution function f_α for an extrapolated water height is calculated by the equilibrium distribution function f_α^{eq}.

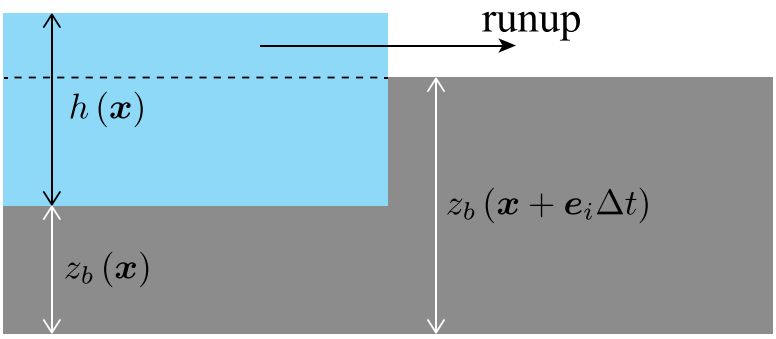

Fig. 3. Schematic diagram of the moving boundary condition for runup and rundown simulation.

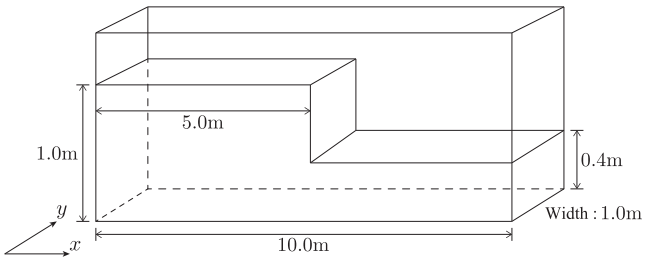

Fig. 4. Initial setting for the dam break flow.

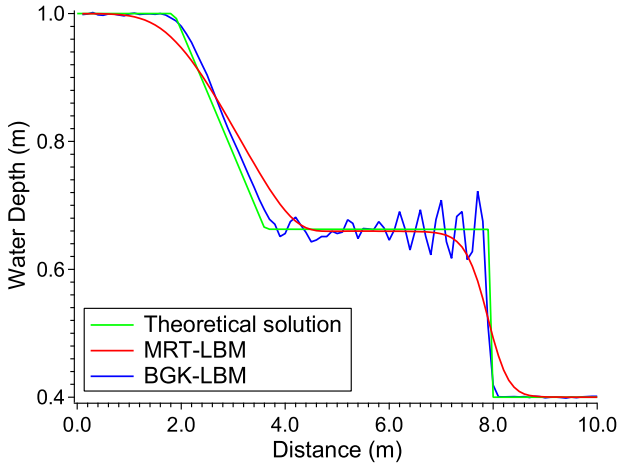

Fig. 5. Comparison of the total water depth of the dam break flow between the BGK and MRT models at $t = 1.0$ s (Case 1).

Otherwise, we apply the bounce-back condition for the neighbouring wetting grid when a grid is drying to achieve the no-slip condition. The bounce-back condition for the distribution function f_α is given as:

$$f_\alpha(\boldsymbol{x}, t+\Delta t) = f_{\bar{\alpha}}(\boldsymbol{x}, t), \tag{40}$$

where $\bar{\alpha}$ is the index that satisfies $e_{\bar{\alpha}} = -e_\alpha$.

4. Verification in classical benchmark problems

4.1. A dam break flow

We simulated the dam break flow to compare the characteristic results of the BGK and MRT models. The dam break is a popular benchmark problem for the numerical test of the nonlinear shallow water equations. Fig. 4 shows the initial conditions. The boundary condition of the sidewall is given by the bounce-back condition as a no-slip boundary. We applied the turbulence model to both the BGK and MRT models.

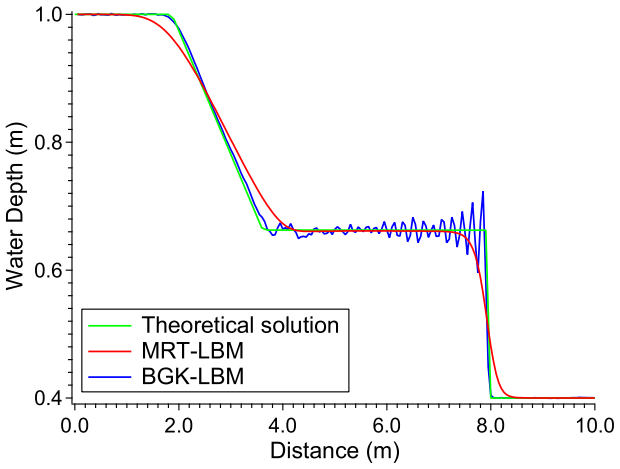

Fig. 6. Comparison of the total water depth of the dam break flow between the BGK and MRT models at $t = 1.0$ s (Case 2).

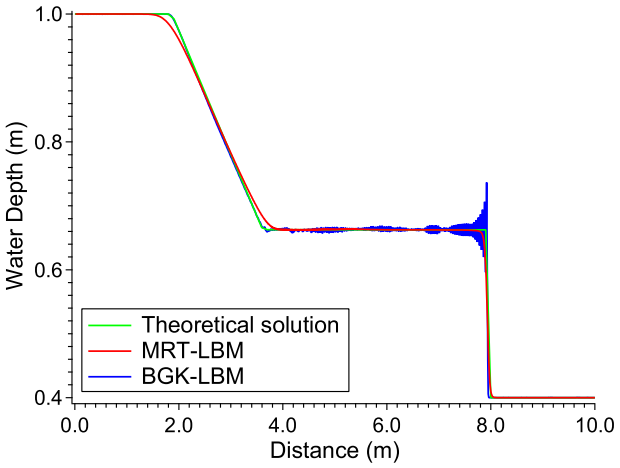

Fig. 7. Comparison of the total water depth of the dam break flow between the BGK and MRT models at $t = 1.0$ s (Case 3).

For this benchmark, an analytical solution is obtained $t = 1$ s after the dam break. We compared the numerical solution with the analytical solution. Table 1 lists the calculation parameters. We set the kinematic viscosity coefficient $\nu = 1.0 \times 10^{-6}$ m^2/s assuming real-world water. The time step Δt is set to $\Delta x/\Delta t = 10.0$ m/s so that the Courant number is sufficiently larger than the wave speed $\sqrt{g h_{\max}} = 3.13$ m/s. In this simulation, τ is very close to 0.5 (e.g., $\tau = 0.5 + 3.0 \times 10^{-6}$ in Case

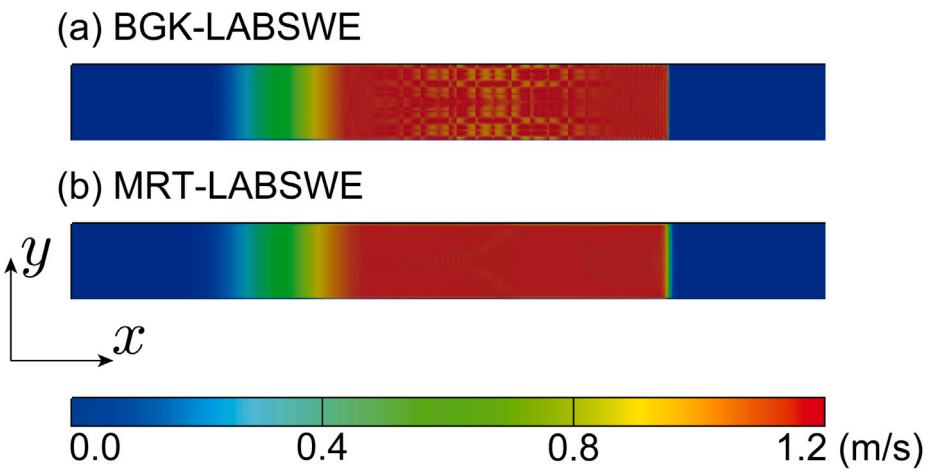

Fig. 8. Snapshots of the velocity of the dam break flow obtained by the BGK and MRT models at $t = 1.0$ s (Case 3).

Table 1
Calculation parameters for the dam break flow. It is noted that s_1 is used only for the MRT model.

Case	Resolution	Δx (m)	Δt (s)	τ	s_1
Case 1	100 × 10	0.1	0.01	$0.5 + 3.0 \times 10^{-6}$	1.0
Case 2	200 × 20	0.05	0.005	$0.5 + 6.0 \times 10^{-6}$	1.0
Case 3	1000 × 100	0.01	0.001	$0.5 + 3.0 \times 10^{-5}$	1.0

1). We verified the computational results with the proposed approach under these challenging conditions.

Figs. 5, 6, and 7 compare the numerical and analytical solutions for the water depth in Cases 1, 2, and 3, respectively. Overall, the BGK model results show large numerical oscillations at the front of the wave. The oscillations due to sound waves are more pronounced when the kinematic viscosity is small because the bulk viscosity in the BGK model is approximately twice the kinematic viscosity. The bulk viscosity is equal to the kinematic viscosity in the BGK model. On the other hand, the MRT model suppresses the oscillations because the bulk viscosity is set to larger values than the kinematic viscosity. Table 1 shows that the relaxation time τ is close to 0.5 in this simulation, which makes the calculation prone to instability. The addition of eddy viscosity increases the local relaxation time, even in the BGK model, making the calculations more stable, but the bulk viscosity remains small and the water depth is considered to oscillate violently. The MRT model is similarly prone to calculation instability when the relaxation time is very close to 0.5, to which the eddy kinematic viscosity is locally added to avoid numerical instability for small kinematic viscosity. In addition, the MRT model allows the bulk viscosity to be set independently of the kinematic viscosity so that the calculations can be performed stably and there is no oscillation in the high-resolution cases. An approach to avoid numerical instability due to relaxation time by locally adding eddy viscosity with a large bulk viscosity set by the MRT model is considered adequate to perform calculations for low-viscosity fluids in the LBM.

However, the MRT model results are significantly lower at the discontinuity points when the grid size is coarse, as shown in Fig. 5. Through this benchmark test, we found that the MRT model is in good agreement with the analytical solution while suppressing the numerical oscillation when the resolution of Case 3 is secured.

Fig. 8 shows a snapshot of the velocity in Case 3 at $t = 1.0$ s. The results of the BGK model show an unstable distribution in the large velocity range. While this instability does not invalidate the simulation, it is desirable to minimize it. The results of the MRT model are very stable and smooth, even though the velocity near the wavefront is slightly decreased, as in the depth results. From this discussion, we conclude that the MRT model is numerically more stable than the BGK model, even when the kinematic viscosity is small. However, excessive bulk viscosity at low resolution reduces the calculation accuracy. There is no unique method for determining the appropriate bulk viscosity for any simulation. Rather, this parameter must be verified by trial and error.

4.2. Flow around a square cylinder

We simulated the flow around a square cylinder (Lyn et al., 1995). This benchmark is often used to verify the reproducibility of the vortex behind a structure in a high Reynolds number flow. Fig. 9 shows the initial conditions. Note that the origin of the x- and y-axes is the centre of the structure. The flow velocity u_x was given as $u_x = 0.535$ m/s from the left-hand boundary, and the right-hand boundary was a non-reflecting boundary. The upper and lower boundary conditions were given as slip boundaries with the mirror scheme on the distribution function. The semislip boundary condition (Zhou, 2004) was applied at the boundary of the square cylinder to conduct a correct turbulence simulation with a Manning's coefficient of 0.006. The bed slope was defined as a plane with a Manning's coefficient of 0.009. The initial still water depth h_0 was 4 m.

In this benchmark, the Reynolds number is defined as:

$$\mathrm{Re} = \frac{UL}{\nu}. \tag{41}$$

We defined the length of the square cylinder to be $L = 1$ m, and this was the characteristic length. The x-axis velocity was initialized as the characteristic velocity $u_x = 0.535$ m/s, whereas $u_y = 0.0$ m/s. The kinematic viscosity ν was $\nu = 2.5 \times 10^{-5}$ m^2/s to obtain the Reynolds number Re = 21400.

Table 2 shows the calculation parameters. Three simulation cases with different grid sizes were examined to study the dependence of the simulated vortex behaviour on the spatial resolution. The total simulation time was 10 min in all cases. This simulation was performed for a long time to investigate whether the LBM with the SGS model is stable in tsunami simulations. The time step interval Δt was set to the largest value at which the calculation could be stably performed.

Figs. 10, 11, and 12 show the velocity profile for each direction after 10 min. In all cases, u_x near the top and bottom boundary slips because the mirror condition is imposed. On the other hand, u_y remains 0. The simulation results accurately reproduce the appearance of the Karman vortex behind the structure in high Reynolds number flows. Case 1 shows the regular formation of the Karman vortex, even after 10 min of simulation, while the flow gradually becomes irregular in Case 2 and is completely irregular in Case 3.

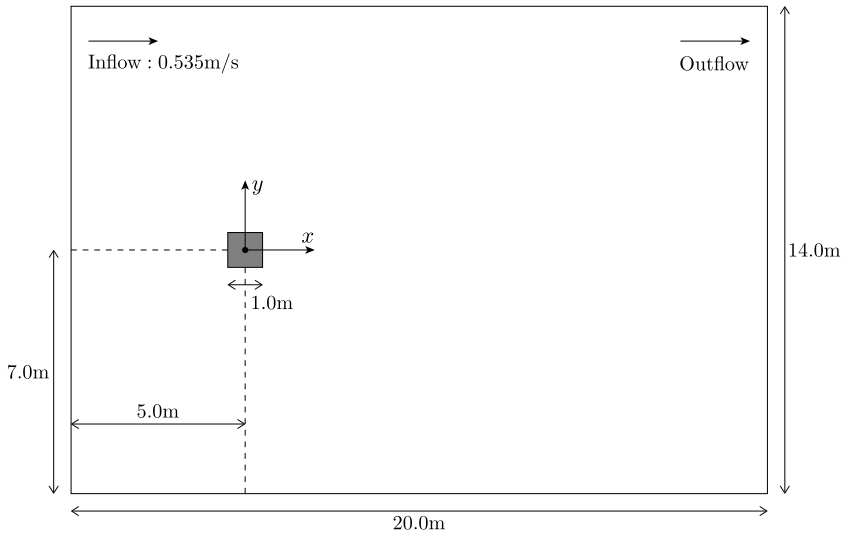

Fig. 9. Initial setup for the square cylinder flow problem.

Table 2
Calculation parameters for the square cylinder flow problem.

Case	Resolution	Δx (m)	Iterations	Δt (s)	τ	s_1
Case 1	200 × 140	0.1	6.0×10^5	0.001	$0.5 + 7.5 \times 10^{-6}$	1.0
Case 2	400 × 280	0.05	6.0×10^5	0.001	$0.5 + 3.0 \times 10^{-5}$	1.0
Case 3	800 × 560	0.025	1.2×10^6	0.0005	$0.5 + 6.0 \times 10^{-5}$	1.0

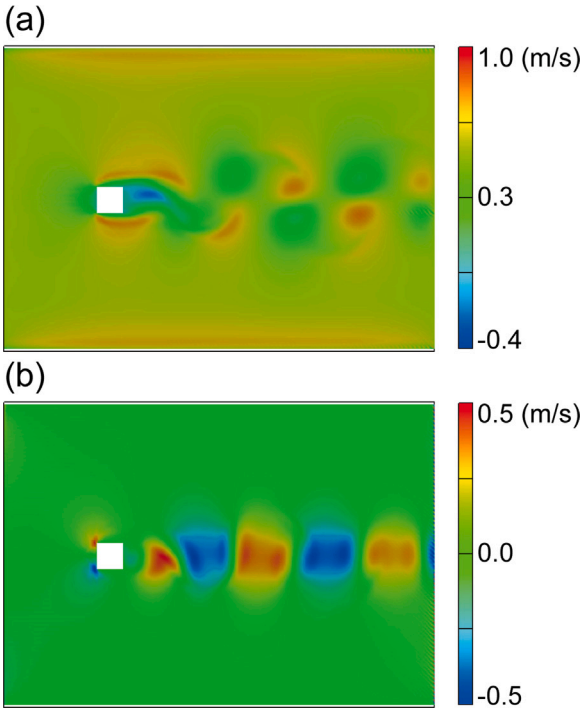

Fig. 10. Velocity profiles of the square cylinder flow (Case 1): (a) u_x, (b) u_y.

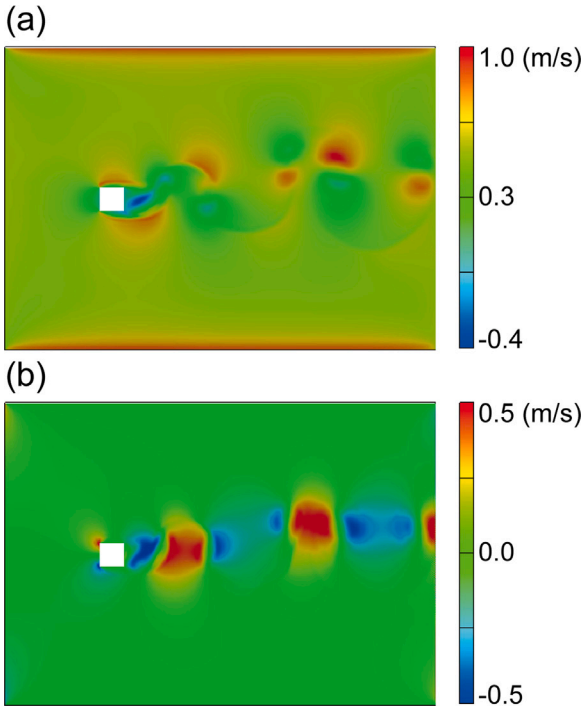

Fig. 11. Velocity profiles of the square cylinder flow (Case 2): (a) u_x, (b) u_y.

In Case 1, u_x shows a slight oscillation at the outlet boundary. This oscillation is corrected in Case 2 and Case 3, where the spacing resolution is finer. Therefore, it is considered a numerical oscillation that arises due to the coarse grid size. It was found that in the analysis of high Reynolds number flows, if sufficient spatial resolution is not ensured, the flow velocity oscillates, which affects the computational domain.

The slip velocity u_x near the upper and lower walls is considered to be influenced by the setting of the time step interval Δt. The slip velocity is stronger in Case 2 than in Case 3, where the time step interval Δt is smaller than in the other two cases. In this study, we focused on verifying the numerical results with the spatial grid spacing Δx. In terms of turbulence analysis near the wall, verifying the results regarding time step interval Δt is an issue for the next step.

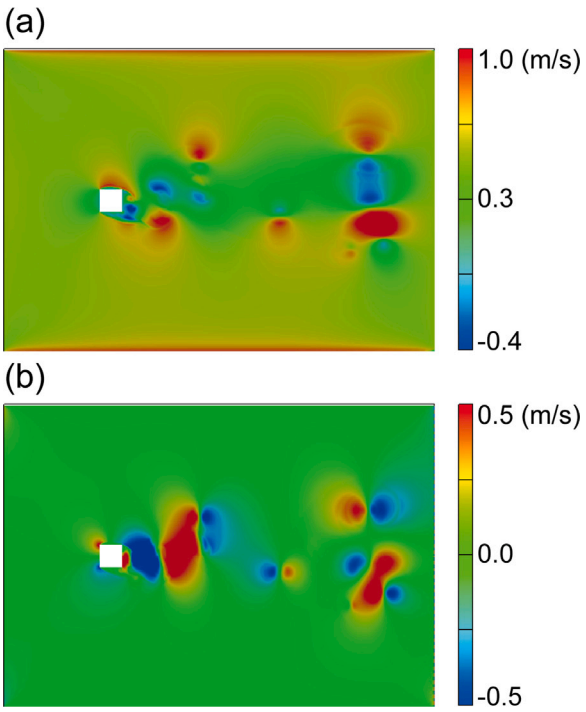

Fig. 12. Velocity profiles of the square cylinder flow (Case 3): (a) u_x, (b) u_y.

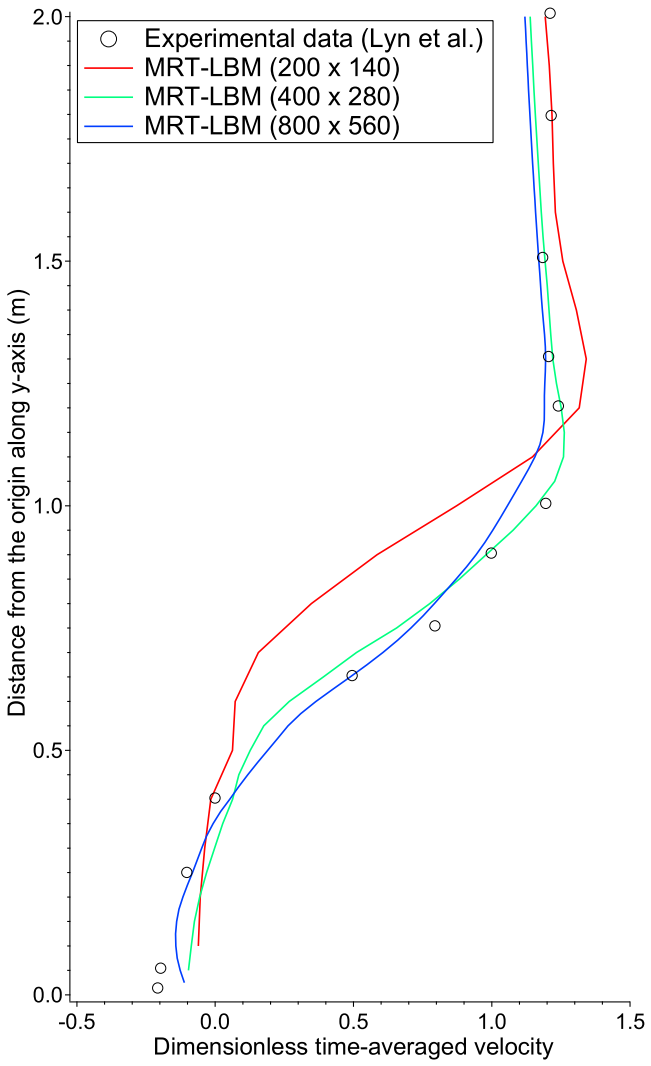

Fig. 13. Time-averaged dimensionless velocity u_x of the square cylinder flow along the y-axis at $x = 1.0$ m.

Fig. 13 presents a plot of the time-averaged u_x at $x = 1.0$ m along the y-axis. The simulation results are consistent with the experimental results for the finer spatial resolution in Case 2 and Case 3. Since the results of Case 2 converge to the results of Case 3, we consider that the MRT-LABSWE with the SGS model is a scheme that shows convergence in accuracy with respect to spatial resolution.

In this study, we found that the MRT-LABSWE with the SGS model can stably perform high Reynolds number flow simulations for a long time and obtains results consistent with the experimental time-averaged velocities. Therefore, this approach is highly applicable to real-world tsunami simulations.

4.3. A two-dimensional cavity flow

We simulated a two-dimensional lid-driven cavity flow in high Reynolds number flows (Ghia et al., 1982; Erturk et al., 2005). This system is typically used as a benchmark test for the NS equation. Fig. 14 shows the initial setup. The flow is caused by the upper wall moving to the right at a constant velocity, dragging the fluid along with it. The other walls are no-slip boundaries. By analogy with the numerical solution of the NS equations, the water depth in the two-dimensional model varies only around the corners of the upper wall. Therefore, it is possible to directly compare and verify the velocities obtained from the NS equations with those of the two-dimensional shallow water equations. In this study, the computational accuracy of the MRT-LABSWE in high Reynolds number flows is verified by comparing it with the numerical solutions of the NS equations.

The initial still water depth was $h_0 = 1.0$ m. U is the top-driven velocity, which is the characteristic velocity, and L is the vertical and horizontal length of the cavity, which is the characteristic length. These values were set as $U = 1.0$ m/s and $L = 1.0$ m, respectively, for all Reynolds numbers. The critical Reynolds number for this problem is between 8000 and 8050 with an error of less than 1% (Bruneau and Saad, 2006). Ghia et al. (1982) simulated up to a Reynolds number of 10000 without a turbulence model. Hou et al. (1996) pointed out that most previous work on cavity flow focused on steady-state behaviour. They argued that the LBM differs from previous methods because it calculates time-dependent behaviour. In fact, Hou et al. (1996) proposed a subgrid-scale model in LBM and calculated cavity flow with a Reynolds number of 10000 using a turbulence model to show its unsteady behaviour and to study the Smagorinsky constant. In the present study, we follow the results of Hou et al. (1996) and carry out calculations with a subgrid-scale model for a Reynolds number of 10000. LABSWE has been verified for this benchmark for Reynolds numbers of up to 10000 (Liu et al., 2012). We extended our simulation up to $\mathrm{Re} = 20000$. Table 3 shows the calculation conditions and parameters. The Reynolds number, which is defined as $\mathrm{Re} = UL/\nu$, was set to 10000, 15000, and 20000. The velocities were verified after 30 min of simulation.

Fig. 15 shows the spatial distribution of the eddy viscosity ν_e at $t = 30$ min for the $\mathrm{Re} = 10000$ case. The result is obtained on a spatial resolution of $(x, y) = (512, 512)$. The eddy viscosity ν_e is large near the velocity boundary at the top lid and other wall boundaries. On the other hand, ν_e is almost zero in the centre of the cavity. We consider that the turbulence model calculates the eddy viscosity appropriately at the flow fields where the turbulence is significant. Figs. 16, 17, and 18 are presented to compare the dimensionless velocity profiles along a vertical line and a horizontal line. The MRT model results are consistent with the numerical results of a previous study. It is confirmed that

Table 3
Calculation parameters for the cavity flow.

Re	Resolution	Δx (m)	Calculation step	Δt (s)	τ	s_1
10000	128 × 128	7.81×10^{-3}	3.6×10^{6}	5.0×10^{-4}	0.50246	1.0
	256 × 256	3.91×10^{-3}	3.6×10^{6}	5.0×10^{-4}	0.50983	1.0
	512 × 512	1.95×10^{-3}	7.2×10^{6}	2.5×10^{-4}	0.51966	1.0
15000	128 × 128	7.81×10^{-3}	3.6×10^{6}	5.0×10^{-4}	0.50164	1.0
	256 × 256	3.91×10^{-3}	3.6×10^{6}	5.0×10^{-4}	0.50655	1.0
	512 × 512	1.95×10^{-3}	7.2×10^{6}	2.5×10^{-4}	0.51311	1.0
20000	128 × 128	7.81×10^{-3}	3.6×10^{6}	5.0×10^{-4}	0.50123	1.0
	256 × 256	3.91×10^{-3}	3.6×10^{6}	5.0×10^{-4}	0.50492	1.0
	512 × 512	1.95×10^{-3}	7.2×10^{6}	2.5×10^{-4}	0.50983	1.0

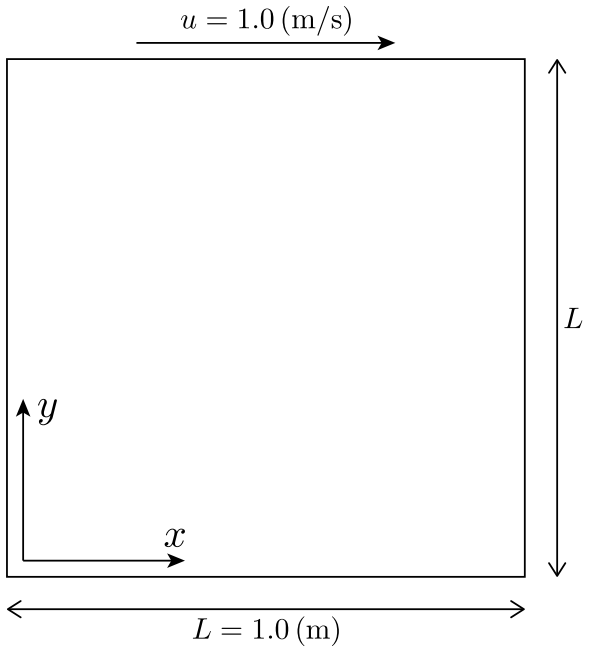

Fig. 14. Initial setup for the cavity flow.

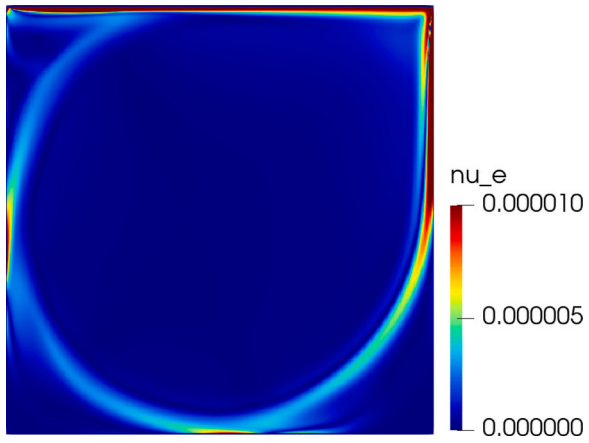

Fig. 15. The spatial profile of the eddy viscosity ν_e (m^2/s) of Re = 10000 after 30 min. The resolution is $(x, y) = (512, 512)$.

the results of the MRT model approach those of previous studies when the spatial resolution increases, particularly near the boundaries. The convergence behaviour of the MRT model with the SGS model depends on the size of the computation grid. This is an important factor in determining the applicability of the model to other problems from an engineering perspective.

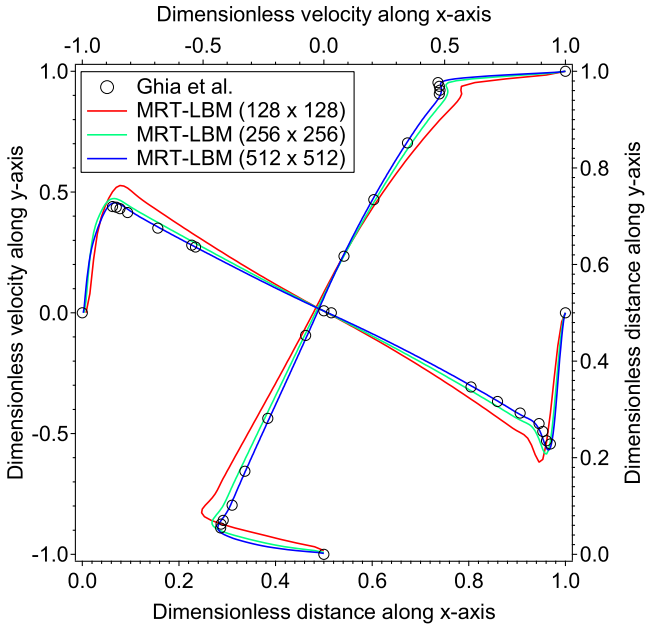

Fig. 16. Velocity profile of the cavity flow along the centre line (Re = 10000).

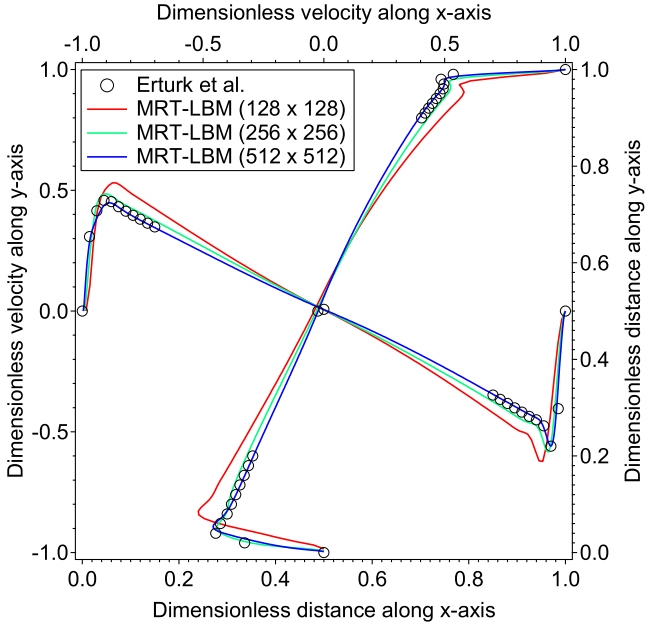

Fig. 17. Velocity profile of the cavity flow along the centre line (Re = 15000).

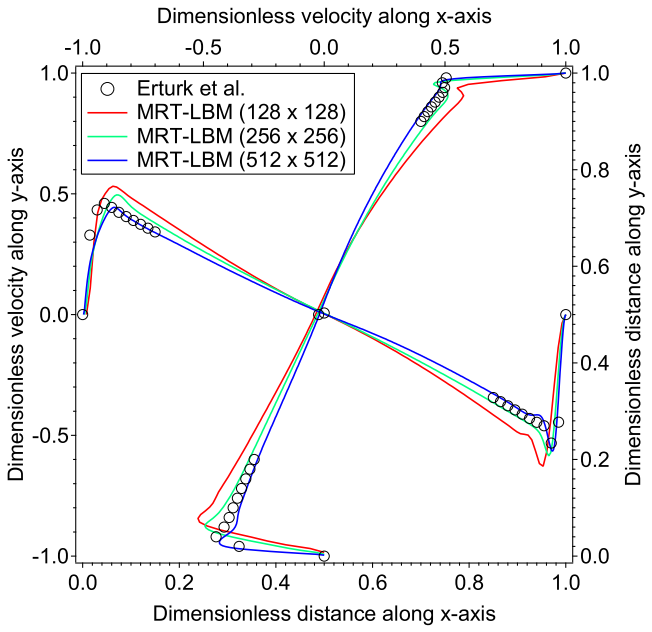

Fig. 18. Velocity profile of the cavity flow along the centre line (Re = 20000).

5. Simulation of the 2011 tsunami off the Pacific coast caused by the Tohoku earthquake

The LBM for tsunami simulation models described in Section 3 was applied to simulate the 2011 tsunami off the Pacific coast caused by the Tohoku earthquake in Onagawa town, Miyagi prefecture, to verify the applicability of the LBM to real-world tsunami simulation. Onagawa town was hit by the tsunami 35 min after the earthquake. The tsunami killed 816 people and left 125 missing. At least six reinforced concrete (RC) and steel buildings were overturned or washed away, causing extensive damage to the area (Koshimura et al., 2013, 2014). In addition, Onagawa town contains the Onagawa nuclear power station. Numerical simulations are critical in the nuclear engineering field for understanding tsunamis and developing tsunami mitigation strategies. In this study, we demonstrate that the results obtained by the LBM simulations are as accurate as those obtained by the conventional FDM simulations that are widely used for tsunami simulation. For the cases where the accuracy of the LBM is equal to that of FDM, we can state that the LBM has sufficient accuracy for tsunami simulation. In this simulation, we also adopted the MRT model as the collision term in the LBM.

5.1. Numerical results

The initial conditions for the tsunami simulation are described. Fig. 19 shows the computational domain. Five subdomains were set up offshore. The multidomain connections were made to simulate tsunami inundation in Onagawa town. Table 4 shows the calculation parameters. The relaxation time τ was determined by trial and error as the smallest value that can be stably calculated in each domain. On the other hand, it is noted that the eddy relaxation time τ_e is calculated by the procedures described in Section 2.4 and is not determined by trial and error. Δt was determined to satisfy the CFL condition in the 5th subregion. No connection was made for time step Δt. The composite equivalent roughness model (ERM) shown in Eq. (38) was used in subregion 5. For other subregions, a constant Manning's roughness coefficient $n = 0.025$ was used.

We used Tohoku University's Numerical Analysis Model for Investigation of Near-field tsunamis (TUNAMI-N2 model) (Goto et al., 1997)

Table 4
Calculation parameters for the 2011 Tohoku earthquake tsunami simulation.

Sub-region	Resolution	Δx (m)	Δt (s)	τ	s_1
Sub-region 1	1330 × 1632	405.0	0.1	0.5001	1.0
Sub-region 2	419 × 374	135.0	0.1	0.52	1.0
Sub-region 3	558 × 472	45.0	0.1	0.53	1.0
Sub-region 4	776 × 422	15.0	0.1	0.54	1.0
Sub-region 5	680 × 665	5.0	0.1	0.55	1.0

as the FDM model. The time step Δt of FDM was set to the same value as that for the LBM. We used the fault parameters of the Cabinet Office model to calculate the ground motion from Okada's equation (Okada, 1985) and set the initial water level. When this fault model is used to determine the initial water level of the tsunami, it must be updated every 30 s. We updated the water level and initialized the distribution function f_α by the equilibrium distribution function f_α^{eq}. The simulation time was 2.5 h. Figs. 20 and 21 show the points where the waveforms of the FDM and LBM are compared in subregion 1 and subregion 3, respectively. The observed point in subregion 3 is the tide metre at the Onagawa nuclear power station. The applicability of the LBM to real tsunami simulations is demonstrated by comparing the FDM waveforms and maximum inundation depths in subregion 5.

Fig. 22 compares the LBM and FDM waveforms in subregion 1. In this domain, we aim to verify the numerical results of the LBM with the FDM for the same fault model. The LBM results show that the calculations are very stable, even for long simulation times of 2.5 h. In addition, Figs. 22 (a) and (b) show that the LBM results are quite similar to the FDM results at offshore locations. On the other hand, Figs. 22 (h) and (j) show a slight difference in the waveform 60 min after the calculation. The common feature of these points is that they are relatively close to the shore, accounting for the difference in the reproducibility of the reflection waves. This difference occurs because FDM is applied to the moving boundary condition at the wavefront. In contrast, the LBM uses the bounce-back scheme, regardless of the water level in this subregion. Although there are some differences in the treatment of reflection waves due to the different boundary conditions, the reproducibility of the first wave and stability of the calculation over a long time show that LBM is a suitable approach for tsunami propagation simulations.

Fig. 23 compares the tide gauge records and numerical results at the Onagawa nuclear power station. The Sanriku coast, which includes Onagawa town, has a V-shaped bay where tsunami energy converges and is amplified (Koshimura et al., 2013, 2014), so that the first wave heights of more than 10 m were observed at this point. The results of the arrival time and wave height of the first wave determined by the LBM are consistent with the FDM numerical results and observed data. The proposed method can accurately reproduce the increase in the wave height due to the shallow water deformation of tsunamis. In addition, because this region is subregion 3, we successfully constructed a multidomain connection model for real-world tsunami simulations. The applicability of our proposed approach to the analysis of actual tsunami propagation is quite high. However, there is a large difference between the LBM and FDM waveforms after 60 min of calculation at this point. Fig. 21 suggests that the difference is caused by the waves reflected due to the boundary condition. This observation point is nearer the shoreline than the point of the waveform obtained in subregion 1.

Fig. 24 compares the maximum inundation depth of LBM and FDM simulations in subregion 5. The LBM results are consistent with the FDM results. In this region, the equivalent roughness coefficient model is used, and the effect of roughness is accurately incorporated into the LBM. This roughness model is a practical and simple method for representing the effects of houses and bottom friction in tsunami simulations. Thus, the LBM is highly applicable to real-world tsunami simulations because it can be directly applied without special treatment. The accurate calculation of inundation area and depth is essential

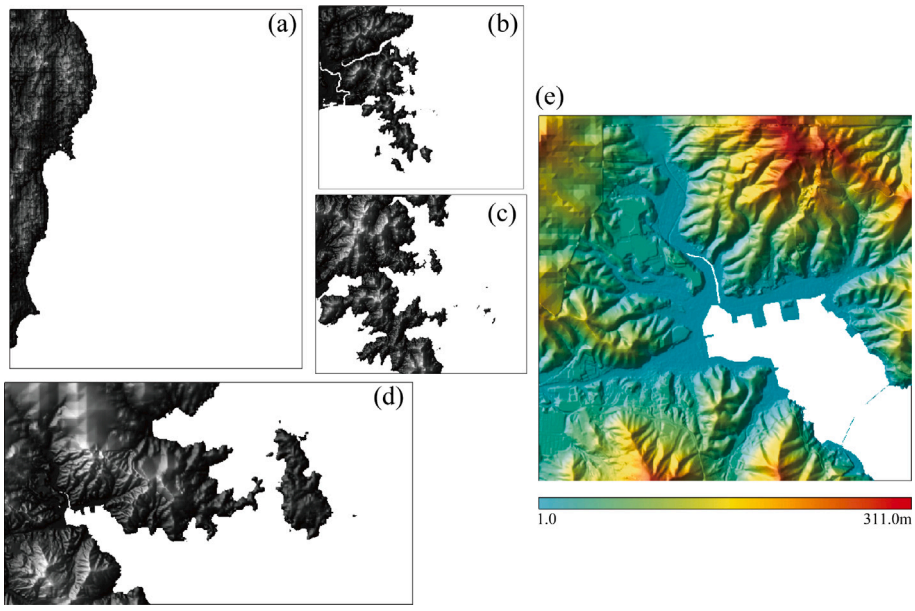

Fig. 19. Subdomains of the 2011 Tohoku earthquake tsunami simulation: (a) subregion 1, (b) subregion 2, (c) subregion 3, (d) subregion 4, (e) subregion 5. Subregion 5 is the inundation area.

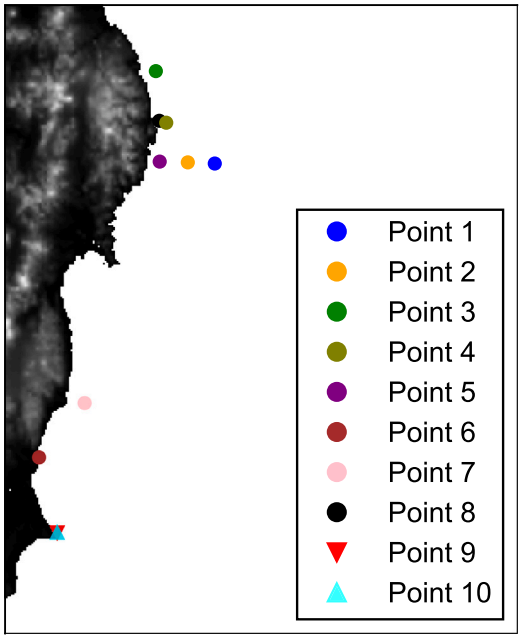

Fig. 20. Measurement points of the waveforms for the comparison between the LBM and FDM in subregion 1.

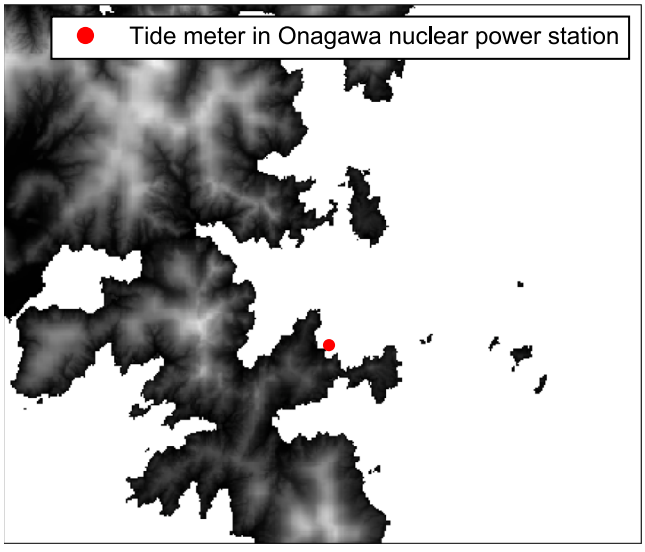

Fig. 21. Measurement point of the waveforms for the comparison between the LBM and FDM in subregion 3. This point is the tide metre at the Onagawa nuclear power station (141.50470 east longitude, 38.40235 north latitude).

for tsunami hazard assessment in nuclear power plants. Based on the above discussion, we have found that the proposed LBM scheme is as accurate as the FDM approach for the given sample fault model. However, there is room for improvement with regard to the reproducibility of reflected waves.

The arbitrariness in the determination of the relaxation time τ remains a challenging issue. This parameter affects both the computational stability and accuracy of the LBM and should be carefully set. We introduced the MRT model that is more stable than the BGK model, even when a smaller relaxation time is considered. However, a large relaxation time may make the waveform less sharp and underestimate the maximum inundation depth. In addition, the viscosities calculated by Eq. (10) with Table 4 are larger than the real-world water viscosity. For example, $\nu = 54.7$ m^2/s in subregion 1. Although the LBM results were as accurate as those of the FDM simulations with this setting, the determination of τ for tsunami modelling is a challenge in terms of uniquely determining the model parameters. Janßen et al. (2015) pointed out the similar problem. They also noted that decreasing the relaxation time did not significantly affect the results. In future work, the applicability of the LBM to real-world tsunami simulation can be improved by determining a factor that automatically determines the relaxation time based on a time step interval Δt and grid size Δx between multiple domains.

6. Conclusions and outlook

In this study, the application of the LBM in real-world tsunami simulation was investigated for a new tsunami hazard assessment method in

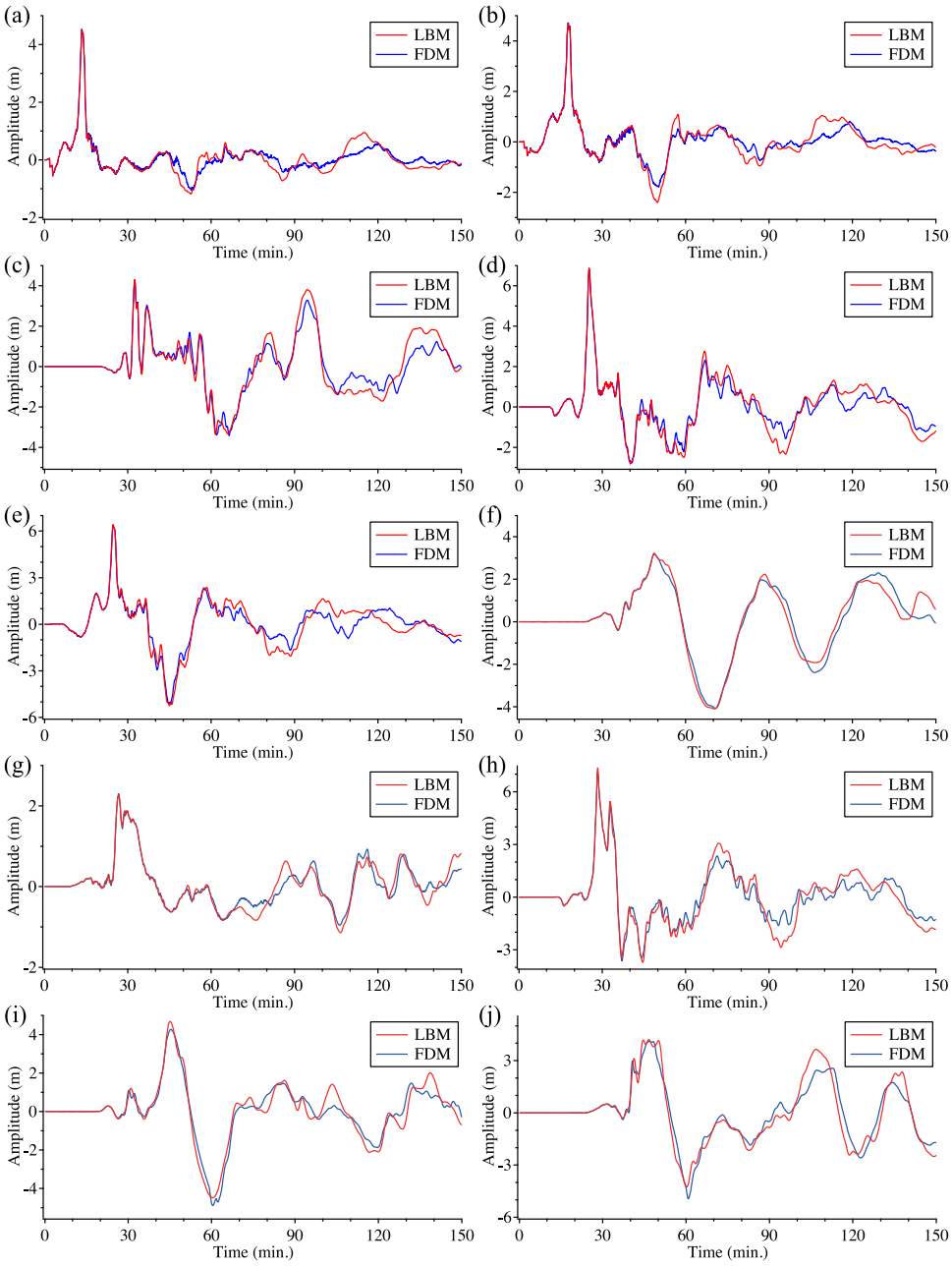

Fig. 22. Comparison of the calculated tsunami waveforms obtained by the LBM and FDM in subregion 1: (a) Point 1, (b) Point 2, (c) Point 3, (d) Point 4, (e) Point 5, (f) Point 6, (g) Point 7, (h) Point 8, (i) Point 9, (j) Point 10.

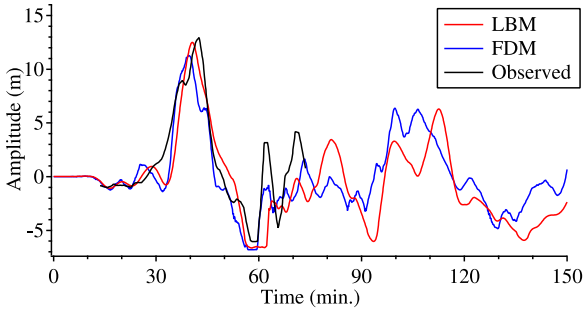

Fig. 23. Comparison of the calculated tsunami waveforms obtained numerically and observed data at the tide metre in Fig. 21.

the nuclear energy field. Three simulations were carried out to demonstrate the validity of the method in high Reynolds number benchmark problems and its applicability to the 2011 Tohoku earthquake tsunami. The main conclusions are listed below.

- In high Reynolds number flows, the BGK model showed oscillations in water depth and velocity, while the MRT model suppressed the numerical oscillations at the wave front. However, when the grid size was excessively coarse, the MRT results were significantly degraded.
- The MRT model was stable even for high Reynolds number flows for a long time. Furthermore, the velocity results were consistent with the results of previous studies (Lyn et al., 1995; Ghia et al., 1982; Erturk et al., 2005). This is a significant result for the development of a robust tsunami simulation model.
- Through the simulation of the 2011 tsunami off the Pacific coast caused by the Tohoku earthquake, we found that the LBM has the

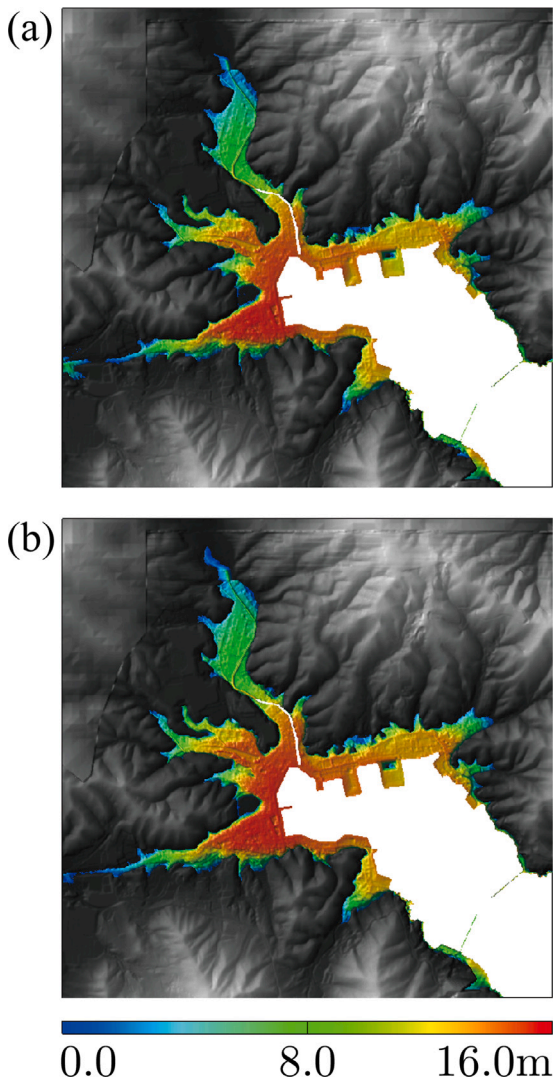

Fig. 24. Maximum inundation depth in subregion 5: (a) LBM, (b) FDM.

same accuracy as the FDM (Goto et al., 1997). The LBM accurately simulated tsunami propagation and inundation.

In this study, we did not investigate the differences in the computational cost between the LBM and FDM, as we primarily focused on the comparison of the computational accuracy of these methods. The LBM was originally designed to be suitable for massively parallel computing using GPUs. It is believed that some ingenuity will be required for memory transfers in carrying out multiregion connections. In addition, appropriate load balancing will also be necessary when performing tsunami runup simulation in an urban area. An efficient implementation of the LBM with the proposed tsunami simulation methods on GPUs is an area for future research.

The LBM has been also actively used in developing the three-dimensional (3D) free-surface model based on the volume-of-fluid (VOF) (Körner et al., 2005; Janssen and Krafczyk, 2010; Janßen and Krafczyk, 2011; Janßen et al., 2013; Sato and Koshimura, 2020; Sato et al., 2022) and the model for the 2D shallow water equations. Moreover, an approach to couple the two models has been proposed (Thürey, 2007). If we can choose between 2D and 3D models according to the required computational accuracy, more efficient and accurate simulations of tsunamis can be achieved. The coupling model of the LBM is expected to be used in tsunami simulations in the future.

CRediT authorship contribution statement

Kenta Sato: Methodology, Software, Validation, Writing – original draft, Visualization. **Koji Kawasaki:** Resources, Writing – review & editing, Funding acquisition. **Shunichi Koshimura:** Conceptualization, Investigation, Writing – review & editing, Supervision, Funding acquisition.

Declaration of competing interest

The authors declare that they have no known competing financial interests or personal relationships that could have appeared to influence the work reported in this paper.

Data availability

No data was used for the research described in the article.

Acknowledgements

This study was supported by JSPS KAKENHI (Grants-in-Aid for Scientific Research). 17H06108 and 21H05001.

References

Baba, T., Takahashi, N., Kaneda, Y., Ando, K., Matsuoka, D., Kato, T., 2015. Parallel implementation of dispersive tsunami wave modeling with a nesting algorithm for the 2011 Tohoku tsunami. Pure Appl. Geophys. 172, 3455–3472. http://dx.doi.org/10.1007/s00024-015-1049-2.

Bhatnagar, P.L., Gross, E.P., Krook, M., 1954. A model for collision processes in gases. I. Small amplitude processes in charged and neutral one-component systems. Phys. Rev. 94, 511–525. http://dx.doi.org/10.1103/PhysRev.94.511.

Bladé, E., Sanz-Ramos, M., Dolz, J., Expósito-Pérez, J.M., Sánchez-Juny, M., 2019. Modelling flood propagation in the service galleries of a nuclear power plant. Nucl. Eng. Des. 352, 110180. http://dx.doi.org/10.1016/j.nucengdes.2019.110180.

Bruneau, C.H., Saad, M., 2006. The 2D lid-driven cavity problem revisited. Comput. & Fluids 35 (3), 326–348. http://dx.doi.org/10.1016/j.compfluid.2004.12.004.

Calore, E., Gabbana, A., Kraus, J., Pellegrini, E., Schifano, S.F., Tripiccione, R., 2016. Massively parallel lattice-Boltzmann codes on large GPU clusters. Parallel Comput. 58, 1–24. http://dx.doi.org/10.1016/j.parco.2016.08.005.

Chen, H., Chen, Y., Hsieh, H.T., Zhang, J., 2007. A lattice Boltzmann modeling of corrosion behavior and oxygen transport in the natural convection lead-alloy flow. Nucl. Eng. Des. 237 (18), 1987–1998. http://dx.doi.org/10.1016/j.nucengdes.2007.01.016.

Chen, H., Chen, S., Matthaeus, W.H., 1992. Recovery of the Navier-Stokes equations using a lattice-gas Boltzmann method. Phys. Rev. A 45, 5339–5342. http://dx.doi.org/10.1103/PhysRevA.45.R5339.

Chen, S., Doolen, G.D., 1998. Lattice Boltzmann method for fluid flows. Annu. Rev. Fluid Mech. 30, 329–364. http://dx.doi.org/10.1146/annurev.fluid.30.1.329.

Cho, Y.S., Jin, S.B., Lee, H.J., 2004. Safety analysis of ulchin nuclear power plant against Nihonkai-Chubu earthquake tsunami. Nucl. Eng. Des. 228 (1–3), 393–400. http://dx.doi.org/10.1016/j.nucengdes.2003.06.015.

Dellar, P.J., 2001. Bulk and shear viscosities in lattice Boltzmann equations. Phys. Rev. E 64, 031203. http://dx.doi.org/10.1103/PhysRevE.64.031203.

D'Humières, D., Ginzburg, I., Krafczyk, M., Lallemand, P., Luo, L.S., 2002. Multiple-relaxation-time lattice Boltzmann models in three dimensions. Philos. Trans. R. Soc. A Math. Phys. Eng. Sci. 360 (1792), 437–451. http://dx.doi.org/10.1098/rsta.2001.0955.

Ebisawa, K., Teragaki, T., Nomura, S., Abe, H., Shigemori, M., Shimomoto, M., 2015. Concept and methodology for evaluating core damage frequency considering failure correlation at multi units and sites and its application. Nucl. Eng. Des. 288, 82–97. http://dx.doi.org/10.1016/j.nucengdes.2015.01.002.

Erturk, E., Corke, T.C., Gökçöl, C., 2005. Numerical solutions of 2-D steady incompressible driven cavity flow at high Reynolds numbers. Internat. J. Numer. Methods Fluids 48 (7), 747–774. http://dx.doi.org/10.1002/fld.953.

Frandsen, J.B., 2008. A simple LBE wave runup model. Prog. Comput. Fluid Dyn. 8 (1–4), 222–232. http://dx.doi.org/10.1504/PCFD.2008.018093.

Gao, D., Chen, Z., Chen, L., 2014. A thermal lattice Boltzmann model for natural convection in porous media under local thermal non-equilibrium conditions. Int. J. Heat Mass Transfer 70, 979–989. http://dx.doi.org/10.1016/j.ijheatmasstransfer.2013.11.050.

Ghia, U., Ghia, K.N., Shin, C.T., 1982. High-Re solutions for incompressible flow using the Navier-Stokes equations and a multigrid method. J. Comput. Phys. 48 (3), 387–411. http://dx.doi.org/10.1016/0021-9991(82)90058-4.

Ghosh, A.K., 2008. Assessment of earthquake-induced tsunami hazard at a power plant site. Nucl. Eng. Des. 238 (7), 1743–1749. http://dx.doi.org/10.1016/j.nucengdes.2007.12.007.

Gingold, R.A., Monaghan, J.J., 1977. Smoothed particle hydrodynamics: Theory and application to non-spherical stars. Mon. Not. R. Astron. Soc. 181 (3), 375–389. http://dx.doi.org/10.1093/mnras/181.3.375.

Goto, C., Ogawa, Y., Shuto, N., Imamura, F., 1997. IUGG/IOC Time Project, Numerical method of tsunami simulation with the leap-frog scheme. In: IOC Manuals and Guides, UNESCO, Paris, p. 130.

Grilli, S.T., Harris, J.C., Tajalli Bakhsh, T.S., Masterlark, T.L., Kyriakopoulos, C., Kirby, J.T., Shi, F., 2013. Numerical simulation of the 2011 Tohoku tsunami based on a new transient FEM co-seismic source: Comparison to far- and near-field observations. Pure Appl. Geophys. 170, 1333–1359. http://dx.doi.org/10.1007/s00024-012-0528-y.

Ha, T., Cho, Y.S., 2015. Tsunami propagation over varying water depths. Ocean Eng. 101, 67–77. http://dx.doi.org/10.1016/j.oceaneng.2015.04.006.

He, X., Chen, S., Zhang, R., 1999. A lattice Boltzmann scheme for incompressible multiphase flow and its application in simulation of Rayleigh-Taylor instability. J. Comput. Phys. 152 (2), 642–663. http://dx.doi.org/10.1006/jcph.1999.6257.

Hou, S., Sterling, J., Chen, S., Doolen, G.D., 1996. A lattice Boltzmann subgrid model for high Reynolds number flows. Fields Inst. Commun. 6, 151–166.

Hussein, A.K., Ashorynejad, H.R., Shikholeslami, M., Sivasankaran, S., 2014. Lattice Boltzmann simulation of natural convection heat transfer in an open enclosure filled with Cu-water nanofluid in a presence of magnetic field. Nucl. Eng. Des. 268, 10–17. http://dx.doi.org/10.1016/j.nucengdes.2013.11.072.

Imai, K., Imamura, F., Iwama, S., 2013. Advanced tsunami computation for urban regions. J. Jap. Soc. Civ. Eng. 69 (2), 311–315. http://dx.doi.org/10.2208/kaigan.69.I_311.

Imamura, F., 1996. Review of tsunami simulation with a finite difference method. In: Yeh, H., Liu, P., Synolakis, C. (Eds.), Long-Wave Run-Up Models. World Scientific, pp. 25–42.

Inamuro, T., Echizen, T., Horai, F., 2018. Validation of an improved lattice Boltzmann method for incompressible two-phase flows. Comput. & Fluids 175, 83–90. http://dx.doi.org/10.1016/j.compfluid.2018.08.017.

Inamuro, T., Yokoyama, T., Tanaka, K., Taniguchi, M., 2016. An improved lattice Boltzmann method for incompressible two-phase flows with large density differences. Comput. & Fluids 137, 55–69. http://dx.doi.org/10.1016/j.compfluid.2016.07.016.

Janßen, C.F., Grilli, S.T., Krafczyk, M., 2013. On enhanced non-linear free surface flow simulations with a hybrid LBM-VOF model. Comput. Math. Appl. 65 (2), 211–229. http://dx.doi.org/10.1016/j.camwa.2012.05.012.

Janssen, C., Krafczyk, M., 2010. A lattice Boltzmann approach for free-surface-flow simulations on non-uniform block-structured grids. Comput. Math. Appl. 59 (7), 2215–2235. http://dx.doi.org/10.1016/j.camwa.2009.08.064.

Janßen, C., Krafczyk, M., 2011. Free surface flow simulations on GPGPUs using the LBM. Comput. Math. Appl. 61 (12), 3549–3563. http://dx.doi.org/10.1016/j.camwa.2011.03.016.

Janßen, C.F., Mierke, D., überrück, M., Gralher, S., Rung, T., 2015. Validation of the GPU-accelerated CFD solver ELBE for free surface flow problems in civil and environmental engineering. Computation 3, 354–385. http://dx.doi.org/10.3390/computation3030354.

Kimura, Y., Wakunaga, T., Yasuda, M., Kimura, H., Kani, N., Mase, H., 2017. Development and verification of wall-flap-gate as tsunami inundation defence for nuclear plants. Nucl. Eng. Des. 323, 299–308. http://dx.doi.org/10.1016/j.nucengdes.2017.03.031.

Kirby, J.T., Shi, F., Tehranirad, B., Harris, J.C., Grilli, S.T., 2013. Dispersive tsunami waves in the ocean: Model equations and sensitivity to dispersion and Coriolis effects. Ocean Model. 62, 39–55. http://dx.doi.org/10.1016/j.ocemod.2012.11.009.

Klar, A., Seaïd, M., Thömmes, G., 2008. Lattice Boltzmann simulation of depth-averaged models in flow hydraulics. Int. J. Comput. Fluid Dyn. 22 (7), 507–522. http://dx.doi.org/10.1080/10618560802243838.

Koda, Y., Lien, F.S., 2015. The lattice Boltzmann method implemented on the GPU to simulate the turbulent flow over a square cylinder confined in a channel. Flow Turbul. Combust. 94 (3), 495–512. http://dx.doi.org/10.1007/s10494-014-9584-y.

Körner, C., Thies, M., Hofmann, T., Thürey, N., Rüde, U., 2005. Lattice Boltzmann model for free surface flow for modeling foaming. J. Stat. Phys. 121 (1–2), 179–196. http://dx.doi.org/10.1007/s10955-005-8879-8.

Koshimura, S., Hayashi, S., Gokon, H., 2013. Lessons from the 2011 Tohoku Earthquake Tsunami Disaster. J. Disaster Res. 8 (4), 549–560. http://dx.doi.org/10.20965/jdr.2013.p0549.

Koshimura, S., Hayashi, S., Gokon, H., 2014. The impact of the 2011 Tohoku earthquake tsunami disaster and implications to the reconstruction. Soils Found. 54 (4), 560–572. http://dx.doi.org/10.1016/j.sandf.2014.06.002.

Koshizuka, S., Oka, Y., 1996. Moving-Particle Semi-implicit method for fragmentation of incompressible fluid. Nucl. Sci. Eng. 123 (3), 421–434. http://dx.doi.org/10.13182/NSE96-A24205.

Krafczyk, M., Tölke, J., Luo, L.S., 2003. Large-eddy simulations with a multiple-relaxation-time LBE model. Internat. J. Modern Phys. B 17 (1–2), 33–39. http://dx.doi.org/10.1142/s0217979203017059.

Lallemand, P., Luo, L.S., 2000. Theory of the lattice Boltzmann method: Dispersion, dissipation, isotropy, Galilean invariance, and stability. Phys. Rev. E 61 (6), 6546–6562. http://dx.doi.org/10.1103/PhysRevE.61.6546.

Lee, T., Lin, C.L., 2005. A stable discretization of the lattice Boltzmann equation for simulation of incompressible two-phase flows at high density ratio. J. Comput. Phys. 206 (1), 16–47. http://dx.doi.org/10.1016/j.jcp.2004.12.001.

Li, S., Huang, P., Li, J., 2015. A modified lattice Boltzmann model for shallow water flows over complex topography. Internat. J. Numer. Methods Fluids 77 (8), 441–458. http://dx.doi.org/10.1002/fld.3991.

Li, Z., Yang, M., Zhang, Y., 2014. A coupled lattice Boltzmann and finite volume method for natural convection simulation. Int. J. Heat Mass Transfer 70, 864–874. http://dx.doi.org/10.1016/j.ijheatmasstransfer.2013.11.077.

Li, Z., Yang, M., Zhang, Y., 2016. Lattice Boltzmann method simulation of 3-D natural convection with double MRT model. Int. J. Heat Mass Transfer 94, 222–238. http://dx.doi.org/10.1016/j.ijheatmasstransfer.2015.11.042.

Liu, H., Li, M., Shu, A., 2012. Large eddy simulation of turbulent shallow water flows using multi-relaxation-time lattice Boltzmann model. Internat. J. Numer. Methods Fluids 70, 1573–1589. http://dx.doi.org/10.1002/fld.3643.

Liu, H., Wang, H., Liu, S., Hu, C., Ding, Y., Zhang, J., 2015. Lattice Boltzmann method for the Saint-Venant equations. J. Hydrol. 524, 411–416. http://dx.doi.org/10.1016/j.jhydrol.2015.03.002.

Liu, H., Zhang, J., Shafiai, S.H., 2016. A second-order treatment to the wet-dry interface of shallow water. J. Hydrol. 536, 514–523. http://dx.doi.org/10.1016/j.jhydrol.2016.03.014.

Liu, H., Zhang, J., Wang, H., Ding, Y., Yi, Y., 2017. Numerical modeling of the tidal wave run-up and the eelgrass habitat at the Laizhou Bay. Ecol. Modell. 360, 378–386. http://dx.doi.org/10.1016/j.ecolmodel.2017.02.025.

Liu, H., Zhou, J.G., 2014. Lattice Boltzmann approach to simulating a wetting-drying front in shallow flows. J. Fluid Mech. 743, 32–59. http://dx.doi.org/10.1017/jfm.2013.682.

Liu, H., Zhou, G.J., Burrows, R., 2009. Lattice Boltzmann model for shallow water flows in curved and meandering channels. Int. J. Comut. Fluid Dyn. 23 (3), 209–220. http://dx.doi.org/10.1080/10618560902754924.

Liu, H., Zhou, J.G., Burrows, R., 2010a. Lattice Boltzmann simulations of the transient shallow water flows. Adv. Water Resour. 33 (4), 387–396. http://dx.doi.org/10.1016/j.advwatres.2010.01.005.

Liu, H., Zhou, J.G., Burrows, R., 2010b. Lattice Boltzmann simulations of the transient shallow water flows. Adv. Water Resour. 33 (4), 387–396. http://dx.doi.org/10.1016/j.advwatres.2010.01.005.

Lucy, L.B., 1977. A numerical approach to the testing of the fission hypothesis. Astron. J. 82, 1013–1024. http://dx.doi.org/10.1086/112164.

Lyn, D.A., Einav, S., Rodi, W., Park, J.H., 1995. A laser-Doppler velocimetry study of ensemble-averaged characteristics of the turbulent near wake of a square cylinder. J. Fluid Mech. 304, 285–319. http://dx.doi.org/10.1017/S0022112095004435.

McNamara, G.R., Zanetti, G., 1988. Use of the Boltzmann equation to simulate lattice-gas automata. Phys. Rev. Lett. 61 (20), 2332–2335. http://dx.doi.org/10.1103/PhysRevLett.61.2332.

MLIT, 2009. National Land Use Classification. Tech. Rep., The Minister of Land, Infrastructure, Transport and Tourism (MLIT).

Morikawa, D., Senadheera, H., Asai, M., 2020. Explicit incompressible smoothed particle hydrodynamics in a multi-GPU environment for large-scale simulations. Comp. Part. Mech. 8, 493–510. http://dx.doi.org/10.1007/s40571-020-00347-0.

Moriyama, K., Furuya, M., 2020. Kinetic energy evaluation for the steam explosion in a shallow pool with a spreading melt layer at the bottom. Nucl. Eng. Des. 360, 110521. http://dx.doi.org/10.1016/j.nucengdes.2020.110521.

Nourgaliev, R.R., Dinh, T.N., Sehgal, B.R., 2002. On lattice Boltzmann modeling of phase transition in an isothermal non-ideal fluid. Nucl. Eng. Des. 211 (2–3), 153–171. http://dx.doi.org/10.1016/S0029-5493(01)00435-6.

Obrecht, C., Kuznik, F., Tourancheau, B., Roux, J.J., 2012. The TheLMA project: A thermal lattice Boltzmann solver for the GPU. Comput. & Fluids 54, 118–126. http://dx.doi.org/10.1016/j.compfluid.2011.10.011.

Obrecht, C., Kuznik, F., Tourancheau, B., Roux, J.J., 2013. Scalable lattice Boltzmann solvers for CUDA GPU clusters. Parallel Comput. 39 (6–7), 259–270. http://dx.doi.org/10.1016/j.parco.2013.04.001.

Ohashi, H., Chen, Y., Akiyama, M., 1995. Simulation of shock-interface interaction using a lattice Boltzmann model. Nucl. Eng. Des. 155 (1–2), 67–71. http://dx.doi.org/10.1016/0029-5493(94)00869-Z.

Oishi, Y., Imamura, F., Sugawara, D., 2015. Near-field tsunami inundation forecast using the parallel TUNAMI-N2 model: Application to the 2011 Tohoku-Oki earthquake combined with source inversions. Geophys. Res. Lett. 42, 1083–1091. http://dx.doi.org/10.1002/2014GL062577.

Okada, Y., 1985. Surface deformation due to shear and tensile faults in a half-space. Bull. Seismol. Soc. Am. 75 (4), 1135–1154. http://dx.doi.org/10.1785/BSSA0750041135.

Peng, Y., Zhou, J.G., Zhang, J.M., Liu, H., 2014. Lattice Boltzmann modeling of shallow water flows over discontinuous beds. Internat. J. Numer. Methods Fluids 75 (8), 608–619. http://dx.doi.org/10.1002/fld.3911.

Podila, K., Chen, Q., Rao, Y., Spencer, J., Buell, J., Morreale, A., David, R., Pfeiffer, P., 2020. CFD simulation of corium flow through an end fitting of a pressurised heavy water reactor. Nucl. Eng. Des. 369, 110850. http://dx.doi.org/10.1016/j.nucengdes.2020.110850.

Qian, Y.H., D'humières, D., Lallemand, P., 1992. Lattice BGK models for Navier - Stokes equation. Europhys. Lett. 17 (6), 479–484. http://dx.doi.org/10.1209/0295-5075/17/6/001.

Ramshaw, J.D., Mousseau, V.A., 1990. Accelerated artificial compressibility method for steady-state incompressible flow calculations. Comput. & Fluids 18 (4), 361–367. http://dx.doi.org/10.1016/0045-7930(90)90027-U.

Rinaldi, P.R., Dari, E.A., Vénere, M.J., Clausse, A., 2012. A Lattice-Boltzmann solver for 3D fluid simulation on GPU. Simul. Model. Pract. Theory 25, 163–171. http://dx.doi.org/10.1016/j.simpat.2012.03.004.

Ryu, S., Kim, Y., Kang, H., Kim, K.K., Ko, S., 2016. Two-dimensional simulation of intermediate-sized bubbles in low viscous liquids using counter diffusion lattice Boltzmann method. Nucl. Eng. Des. 305, 547–558. http://dx.doi.org/10.1016/j.nucengdes.2016.06.001.

Ryu, S., Kim, Y., Yoon, J., Ko, S., 2014. Direct numerical simulation of circular-cap bubbles in low viscous liquids using counter diffusion lattice Boltzmann method. Nucl. Eng. Des. 266, 17–33. http://dx.doi.org/10.1016/j.nucengdes.2013.10.007.

Ryu, S., Ko, S., 2012. Direct numerical simulation of nucleate pool boiling using a two-dimensional lattice Boltzmann method. Nucl. Eng. Des. 248, 248–262. http://dx.doi.org/10.1016/j.nucengdes.2012.03.031.

Saji, G., 2014. Safety goals for seismic and tsunami risks: Lessons learned from the Fukushima Daiichi disaster. Nucl. Eng. Des. 280, 449–463. http://dx.doi.org/10.1016/j.nucengdes.2014.09.013.

Sato, K., Kawasaki, K., Koshimura, S., 2022. A comparative study of the cumulant lattice Boltzmann method in a single-phase free-surface model of violent flows. Comput. & Fluids 236, 105303. http://dx.doi.org/10.1016/j.compfluid.2021.105303.

Sato, K., Koshimura, S., 2020. Validation of the MRT-LBM for three-dimensional free-surface flows: An investigation of the weak compressibility in dam-break benchmarks. Coast. Eng. J. 62 (1), 53–68. http://dx.doi.org/10.1080/21664250.2019.1672124.

Shafiai, S.H., Gohari, A., Ying, B.Y., 2021. Computational study of tsunami inundation using the LABSWETM—Sisko model. Eur. J. Mech. B Fluids 88, 251–263. http://dx.doi.org/10.1016/j.euromechflu.2021.04.010.

Thömmes, G., Seaïd, M., Banda, M.K., 2007. Lattice Boltzmann methods for shallow water flow applications. Internat. J. Numer. Methods Fluids 55 (7), 673–692. http://dx.doi.org/10.1002/fld.1489.

Thürey, N., 2007. Physically Based Animation of Free Surface Flows with the Lattice Boltzmann Method (Ph.D. thesis). University of Erlangen-Nuremberg.

Tiftikçi, A., Kocar, C., 2016. Lattice Boltzmann simulation of flow across a staggered tube bundle array. Nucl. Eng. Des. 300, 135–148. http://dx.doi.org/10.1016/j.nucengdes.2016.01.020.

Tubbs, K.R., Tsai, F.T., 2019. MRT-Lattice Boltzmann model for multilayer shallow water flow. Water 11 (8), 1623. http://dx.doi.org/10.3390/w11081623.

Vallée, C., Lucas, D., Beyer, M., Pietruske, H., Schütz, P., Carl, H., 2010. Experimental CFD grade data for stratified two-phase flows. Nucl. Eng. Des. 240 (9), 2347–2356. http://dx.doi.org/10.1016/j.nucengdes.2009.11.011.

Wang, J., Wang, D., Lallemand, P., Luo, L.S., 2013. Lattice Boltzmann simulations of thermal convective flows in two dimensions. Comput. Math. Appl. 65 (2), 262–286. http://dx.doi.org/10.1016/j.camwa.2012.07.001.

Wang, P., Zhang, Y., Guo, Z., 2017. Numerical study of three-dimensional natural convection in a cubical cavity at high Rayleigh numbers. Int. J. Heat Mass Transfer 113, 217–228. http://dx.doi.org/10.1016/j.ijheatmasstransfer.2017.05.057.

Yang, Z.L., Dinh, T.N., Nourgaliev, R.R., Sehgal, B.R., 2001. Numerical investigation of boiling regime transition mechanism by a Lattice-Boltzmann model. Nucl. Eng. Des. 204 (1–3), 143–153. http://dx.doi.org/10.1016/S0029-5493(00)00309-5.

Yoshida, H., Nagaoka, M., 2010. Multiple-relaxation-time lattice Boltzmann model for the convection and anisotropic diffusion equation. J. Comput. Phys. 229 (20), 7774–7795. http://dx.doi.org/10.1016/j.jcp.2010.06.037.

Zheng, H., Shu, C., Chew, Y., 2006. A lattice Boltzmann model for multiphase flows with large density ratio. J. Comput. Phys. 218 (1), 353–371. http://dx.doi.org/10.1016/j.jcp.2006.02.015.

Zhou, J.G., 2002. A lattice Boltzmann model for the shallow water equations with turbulence modeling. Internat. J. Modern Phys. C 13 (8), 1135–1150. http://dx.doi.org/10.1142/S0129183102003814.

Zhou, J.G., 2004. Lattice Boltzmann Methods for Shallow Water Flows. Springer.

Zhou, J.G., 2011. Enhancement of the LABSWE for shallow water flows. J. Comput. Phys. 230 (2), 394–401. http://dx.doi.org/10.1016/j.jcp.2010.09.027.

Zhou, J.G., Borthwick, A.G., 2011. Lattice Boltzmann method for variable density shallow water equations. Comput. & Fluids 49 (1), 146–149. http://dx.doi.org/10.1016/j.compfluid.2011.05.007.

Zhou, J.G., Liu, H., 2013. Determination of bed elevation in the enhanced lattice Boltzmann method for the shallow-water equations. Phys. Rev. E 88 (2), 1–6. http://dx.doi.org/10.1103/PhysRevE.88.023302.